Article

Dynamics, interactions and delays of the 2019 Ridgecrest rupture sequence

https://doi.org/10.1038/s41586-023-05985-x

Received: 28 July 2022

Accepted: 20 March 2023

Published online: 24 May 2023

Check for updates

Taufiq Taufiqurrahman[1], Alice-Agnes Gabriel[1,2]✉, Duo Li[1], Thomas Ulrich[1], Bo Li[1], Sara Carena[1], Alessandro Verdecchia[3,4] & František Gallovič[5]

The observational difficulties and the complexity of earthquake physics have rendered seismic hazard assessment largely empirical. Despite increasingly high-quality geodetic, seismic and field observations, data-driven earthquake imaging yields stark differences and physics-based models explaining all observed dynamic complexities are elusive. Here we present data-assimilated three-dimensional dynamic rupture models of California's biggest earthquakes in more than 20 years: the moment magnitude (M_w) 6.4 Searles Valley and M_w 7.1 Ridgecrest sequence, which ruptured multiple segments of a non-vertical quasi-orthogonal conjugate fault system[1]. Our models use supercomputing to find the link between the two earthquakes. We explain strong-motion, teleseismic, field mapping, high-rate global positioning system and space geodetic datasets with earthquake physics. We find that regional structure, ambient long- and short-term stress, and dynamic and static fault system interactions driven by overpressurized fluids and low dynamic friction are conjointly crucial to understand the dynamics and delays of the sequence. We demonstrate that a joint physics-based and data-driven approach can be used to determine the mechanics of complex fault systems and earthquake sequences when reconciling dense earthquake recordings, three-dimensional regional structure and stress models. We foresee that physics-based interpretation of big observational datasets will have a transformative impact on future geohazard mitigation.

The moment magnitude (M_w) 6.4 Searles Valley foreshock and the M_w 7.1 Ridgecrest mainshock that occurred in California on 4 and 5 July 2019 are prominent examples of large, well-recorded earthquakes[1–3] and provide an opportunity to advance our understanding of the mechanics and regional hazard of active multi-fault systems. The sequence cascaded across hierarchically interlaced antithetic faults[4], part of the presumably immature Eastern California Shear Zone (ECSZ). The ECSZ accommodates an increasing fraction of regional tectonic forces[5] while developing into a major tectonic boundary. Multiscale block rotation in its transtensional deformation regime leads to ubiquitous conjugate and subparallel strike-slip faulting, which may promote the initiation and segmentation of large earthquakes, which can occur simultaneously or in quick succession[6,7].

Both earthquakes were highly complex[8], including likely fault reactivation[9,10]. Peculiarly, the largest events were set apart in time by 34 hours[11,12] while driving aftershocks, shallow aseismic creep and swarm activity[13,14]. Numerous inversion-based earthquake models (for example, ref. 15) use this exceptionally high-quality dataset, but, despite the good coverage of geodetic and seismic observations, the proposed slip models and their interpretations differ starkly. It is still a matter of debate which fault segments actively slipped and which regional conditions promote the general occurrence of conjugate earthquake cascades. Data-driven approaches are inherently limited in their ability to uniquely resolve fault interactions and are specifically challenged by multiple slip episodes occurring close in time and activating partially overlapping fault segments, all common characteristics of earthquake sequences in multi-fault systems. Thus, a unifying approach, capable of jointly explaining independent datasets and intriguing dynamic features, such as the delayed triggering of the mainshock, is required, but remains elusive.

Here we present a tightly data-constrained and physics-based approach that disentangles the competing and non-unique views[15] of the Ridgecrest foreshock and mainshock and their inter-relationship, with general implications for the often underestimated hazard posed by multi-fault earthquakes. We address the fundamental questions about the sequence in a data-fused yet physics-based manner, to determine what governs the initiation, propagation and arrest of coseismic slip on immature, geometrically complex faults, how earthquake sequences dynamically interact across multi-fault systems, and the role of heterogeneity in the subsurface and in the ambient stress field, including heterogeneity from historical and recent events, for the dynamics of large earthquakes.

Our supercomputing-empowered three-dimensional (3D) linked foreshock–mainshock dynamic rupture models (Methods) provide insight into the multi-stage dynamics of how an immature conjugate fault system yields and slides. We reveal foreshock and mainshock

[1]Department of Earth and Environmental Sciences, Ludwig-Maximilians-Universität München, Munich, Germany. [2]Institute of Geophysics and Planetary Physics, Scripps Institution of Oceanography, University of California San Diego, La Jolla, CA, USA. [3]Department of Earth and Planetary Sciences, McGill University, Montreal, Quebec, Canada. [4]Institute of Geology, Mineralogy and Geophysics, Ruhr-University Bochum, Bochum, Germany. [5]Department of Geophysics, Faculty of Mathematics and Physics, Charles University, Prague, Czech Republic. ✉e-mail: algabriel@ucsd.edu

dynamics that are characterized by simultaneous rupture of conjugate faults, mixed crack- and pulse-like propagation, and strong interseismic interaction. By combining multidisciplinary and multiscale observations, we constrain the mechanical properties of the fault system to be statically strong but dynamically weak. Dynamic rupture of a statically-strong-yet-dynamically-weak fault system is driven by overpressurized fluids and low dynamic friction in our models. This concept, first proposed to reconcile the San Andreas heat flow paradox[16], allows faults to operate at low average prestress while facilitating multi-fault cascading rupture dynamics[17]. Although dynamic fault weakening may not operate during all natural earthquakes and other mechanisms such as frictional heterogeneity may explain multi-fault ruptures, we show that the interplay of 3D fault stress, strength and geometries remains important even if all faults are dynamically weak.

We demonstrate how a 3D stress model fusing regional tectonics and coseismic and postseismic stress changes of historical earthquakes drives and delays an earthquake sequence through space and time. Our multi-fault model unifies dense strong-motion and teleseismic, field mapping, high-rate Global Navigation Satellite System, and space geodetic foreshock and mainshock datasets with earthquake physics. For comparison in the near- and far-field, we also present a frequency-dependent aftershock-calibrated backprojection analysis[18] (Methods) and kinematic parametric source inversion (PSI)[19] (Methods) using strong-motion data, accounting for the geometric fault complexity that we find is required in dynamic modelling.

From tectonics to dynamic rupture

We apply assimilation methods fusing tectonic, structural, coseismic and interseismic data to jointly inform physics-based dynamic rupture simulations. First, integrating interferometric synthetic aperture radar (InSAR), satellite imagery, relocated seismicity and selected focal mechanisms, we construct[20] (Methods) a non-vertical, quasi-orthogonal cross-cutting 3D fault system (Fig. 1). It consists of four geometrically complex fault segments (Supplementary Fig. 1), all of which slip coseismically during either the foreshock or the mainshock or both: three northwest–southeast-trending right-lateral faults, F1, F3 and F4, and a conjugate northeast–southwest-trending left-lateral fault, F2. The largest fault, F3, is helically shaped, consistent with the geometry of deep ductile shear localization[21]. We next embed this fault system in a 3D Earth structure combining a 3D community velocity model[22] (Methods) and a two-dimensional (2D) community stress model[23] representing the regional state of stress in the Southern California upper crust (Fig. 1a and Supplementary Fig. 2). To account for fault-local stress heterogeneity owing to past seismicity, we incorporate a 3D model of the cumulative coseismic and postseismic stress changes of major historical and recent earthquakes spanning approximately the past 1,400 years, extended in the course of this study from ref. 24 (Fig. 1b). We combine the resulting heterogeneous ambient stress model with the linear depth dependence of the effective vertical stress (Methods).

There is little consensus about the effective strength of active faults[25]. We demonstrate that a large frictional strength drop, requiring statically strong but dynamically weak faults (Supplementary Table 2), promotes dynamic cascading of rupture across the Ridgecrest system of vastly varying fault orientations. We use a laboratory-based modern friction law (Methods) that features markedly rate-dependent dynamic weakening[26], while being compatible with the high static frictional strength of rocks and multi-fault cascading rupture dynamics[17]. We introduce depth-dependent frictional parameters to account for shallow (above 1.8-km depth) velocity strengthening and along-fault variations in seismogenic depth, as inferred from aftershock locations[1], decreasing from a maximum of about 11 km near the foreshock hypocentre towards north and south (Supplementary Fig. 3). Overpressurized fault zone fluids, above the hydrostatic pressure gradient, reduce the apparent strength of faults by decreasing the effective normal stress. Our model suggests that the Ridgecrest fault system is embedded in a region of elevated pore fluid pressure, with fluid pressure higher on the foreshock faults than on the mainshock ones (Supplementary Fig. 4).

In dynamic rupture models, the ratio of potential stress drop to frictional breakdown strength (R) is a key parameter controlling earthquake kinematics, dynamic triggering ('cascading') potential and dynamic slip tendency (Methods). We prescribe the prestress relative to strength drop on a virtual, optimally oriented fault within the model domain as $R_0 = 0.8$. This introduces spatially variable relative fault prestress $R \leq R_0$ (Fig. 1c), and brings more optimally oriented fault segments locally close to being critically prestressed. The orientation of all regional principal stress components, the relative magnitude of the intermediate principal stress, the choice of R_0, and the cumulative coseismic and postseismic stress changes (Fig. 1d) together define the complex 3D pre-sequence stress state that governs the dynamics of the sequence. The conjugate fault F2 and central portions of F3 are well oriented, as illustrated by R locally approaching $R_0 = 0.8$, and simultaneously close to critically prestressed, as the ratio of shear to effective normal prestresses is high (Supplementary Fig. 5). In contrast, F1, F4, and the southern and northern parts of F3 show considerably lower R and are therefore further from critical prestress, reflecting geometrical deviation from optimal orientation with respect to the complex 3D stress model.

We use data-inferred key characteristics of both earthquakes, specifically the hypocentre and aftershock locations[1,27], moment release rate[8,28,29], and the delay between foreshock and mainshock, to find the required dynamic parameters R_0, pore fluid pressure and rupture initiation overstress using several systematic dynamic rupture simulations (Methods). We do not invert space geodesy, strong-motion, high-rate global positioning system (GPS) or teleseismic recordings, but use them for retrospective validation of our earthquake source models. Although the need for ad hoc rupture nucleation at prescribed hypocentres is a limitation of dynamic rupture simulations (Methods), analysing the minimum perturbation leading to self-sustained foreshock and mainshock earthquake dynamics matching observations provides insights into the underlying physics of the cascading rupture sequence. We find that our observationally constrained model balances the dynamic viability of sustained foreshock and mainshock dynamic rupture scenarios with realistic stress drop, rupture speed and fault slip.

Foreshock cross-fault earthquake dynamics

Our earthquake model of the M_w 6.4 Searles Valley foreshock features highly complex dynamics across conjugate faults while failing to coseismically trigger the mainshock. Joint seismological and geodetic[30], and conceptual dynamic[31,32] models imply a cross-fault rupture path, initiating as deep slip on a right-lateral fault segment (F1; Fig. 2a) and continuing on an almost orthogonally interlocked left-lateral segment (F2). Although the F2 surface rupture was traced, satellite images[33] give no indication of the surface rupture along F1.

Our spontaneous dynamic rupture simulations reproduce conjugate rupture observations, and find that foreshock–mainshock fault system interactions are important in facilitating the subsequent mainshock dynamics. Rupture initiates (Methods) close to the F1–F2 fault intersection, which may be a general prerequisite for simultaneous rupture of conjugate faults as suggested from field observations[6]. Early and deep right-lateral dynamic rupture across F1 activates the conjugate, critically prestressed left-lateral F2 leading to complex foreshock slip evolution (Fig. 2a and Supplementary Video 1). At 2 s, rupture takes the form of a near-symmetric, circular crack propagating across both faults, but with higher slip rates (up to about 3 m s^{-1}) on F1 (Fig. 2a). At 5 s, slip on F1 spontaneously ceases without reaching the surface owing to this fault's non-optimal orientation and lower-than-critical prestress. In contrast, dynamic rupture on F2 continues to the southwest and

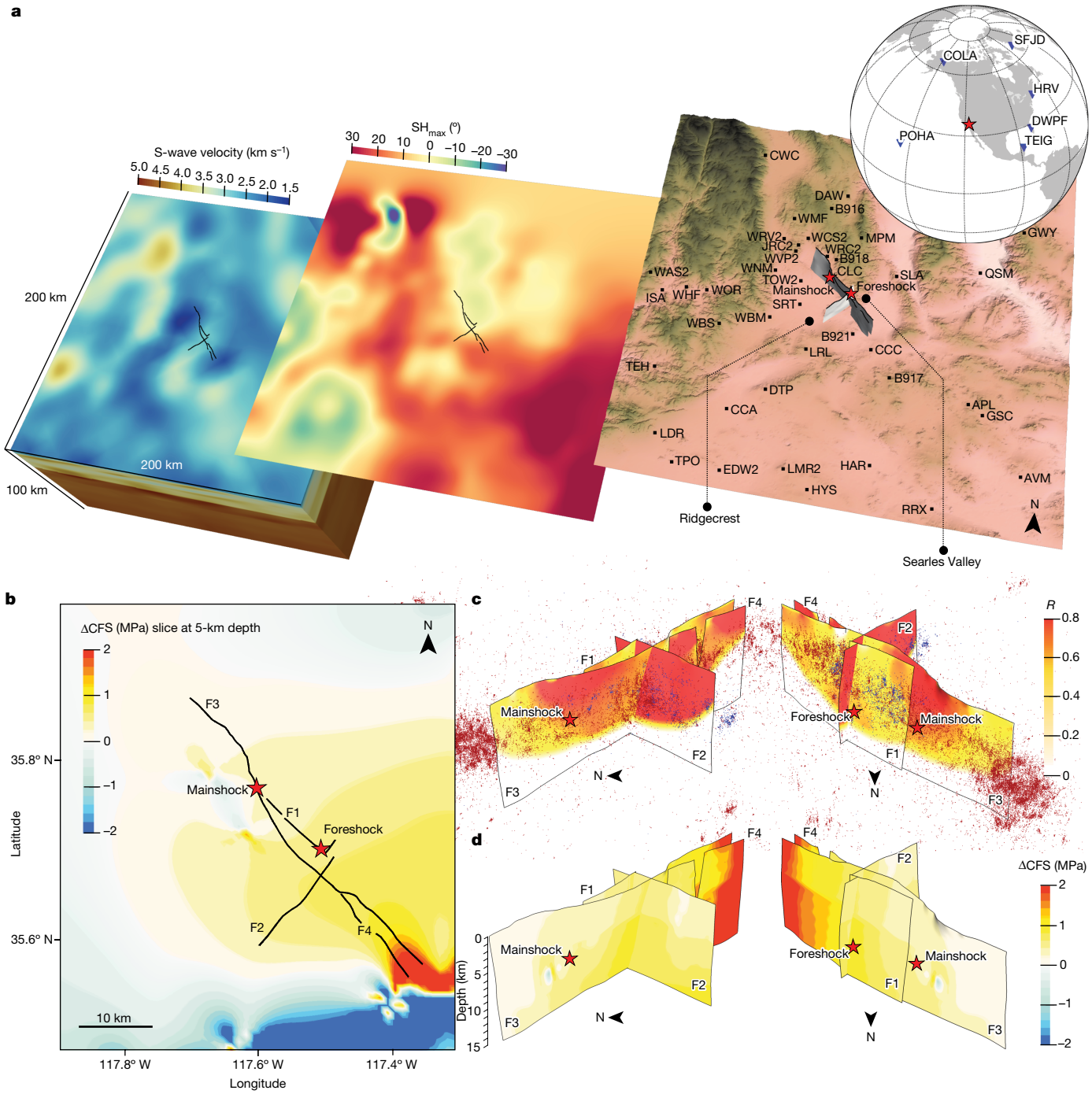

Fig. 1 | Observational constraints for 3D dynamic rupture modelling of the Ridgecrest earthquake sequence. a, The 3D S-wave velocity model (left; CVM-S4.26[22]), the 2D model of maximum horizontal stress orientation SH_{max} (middle; YHSM-2013[23]) and the study region with geometrically complex fault network (black lines) intersecting topography from Shuttle Radar Topography Mission digital elevation model data (right). The chosen strong-motion (black squares, far right) and teleseismic (blue triangles, inset) station locations and codes are shown. **b**, The 3D cumulative Coulomb failure stress change ΔCFS owing to major historical and recent earthquakes (Supplementary Table 1 and Methods), sliced at 5-km depth. **c**, Two perspectives of the relative prestress ratio *R*, which is modulated by fault geometry and heterogeneous ambient stress. The blue and red dots are relocated hypocentres of the foreshock and mainshock aftershocks[1], and the red stars are the foreshock and mainshock hypocentre locations[27]. **d**, ΔCFS resolved on the fault network, assuming a rake of −170° on fault segments F1, F3 and F4, and 0° on F2.

up-dip and breaks the surface, until terminated by pronounced stopping phases. Importantly, F2 rupture takes the form of a narrow slip pulse which re-accumulates a significant amount of shear stress across F2, aiding subsequent reactivation[34] during the mainshock.

The physics-based dynamic model agrees with data-driven kinematic models that assume comparable fault geometries. Figure 2b showcases the overall agreement of the final slip distribution with a newly inferred kinematic PSI of strong-motion data (Methods). The dynamic rupture model yields depth-confined (8–11 km) right-lateral slip on F1 and widespread left-lateral slip on F2 including pronounced surface rupture (Fig. 2b). The maximum fault slip reaches about 1.5 m on F1 near the hypocentre and about 1 m on F2 near the surface. The

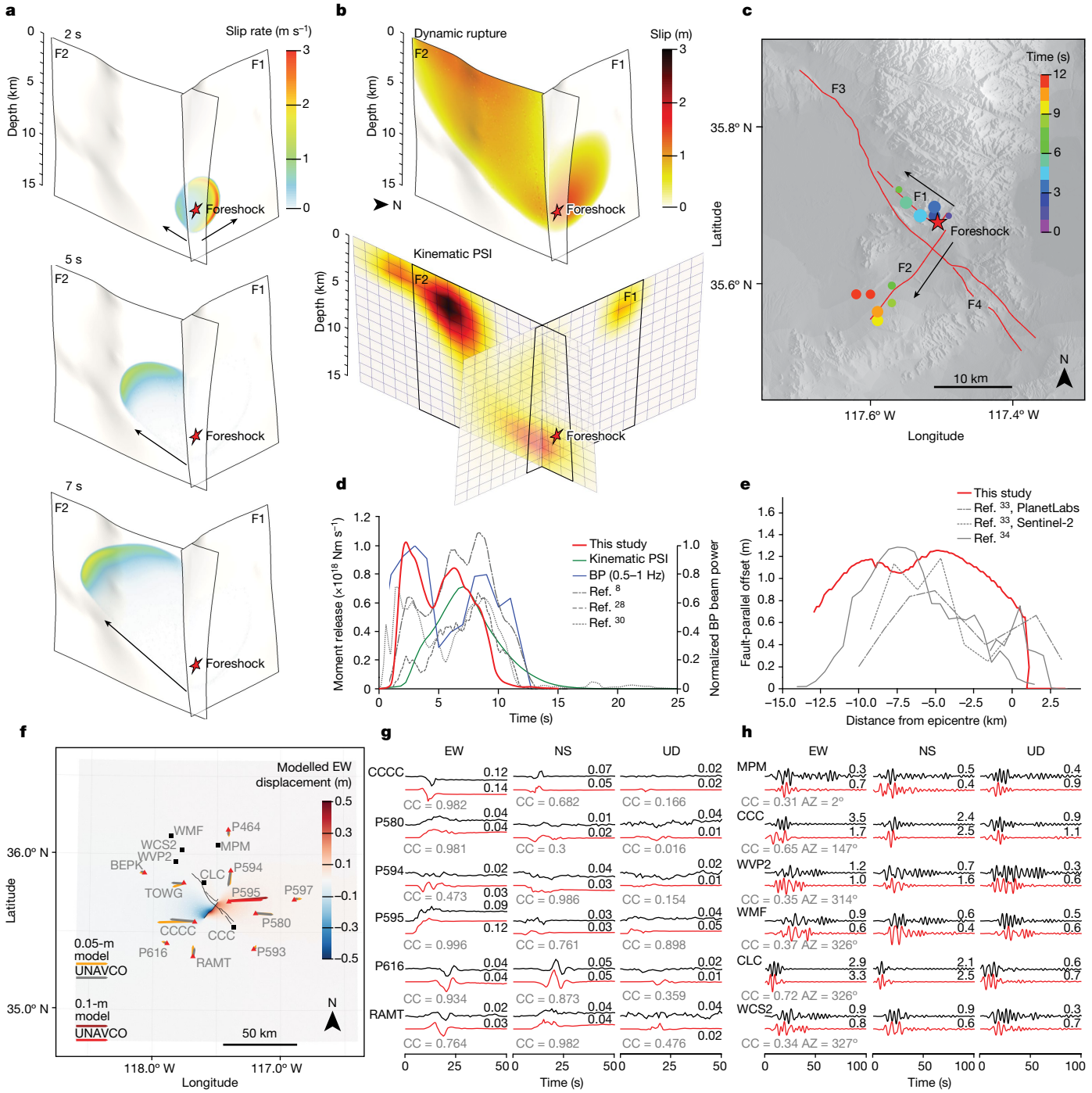

Fig. 2 | Dynamic rupture scenario of the Searles Valley foreshock and comparison with observations. a, Snapshots of absolute slip rate (see also Supplementary Video 1). **b**, Fault slip of the dynamic rupture model (top) and kinematic PSI (bottom). **c**, Aftershock-calibrated backprojection (0.5–1 Hz). The black arrows show the rupture directions. **d**, Dynamic rupture moment release rate and backprojection beam power (BP) compared with kinematic models[8,28,30] including PSI. **e**, Fault-parallel surface offsets along F2 (red is from the dynamic rupture model measured orthogonally across the fault trace 400 m from it, and grey is from the optical images using the orbits of PlanetLabs and Sentinel-2[33]), and on-fault slip estimated from high-resolution optical satellite image correlation[44]. **f**, Horizontal coseismic surface deformation. Orange and red vectors are the modelled static horizontal displacements scaled by 0.05 m and 0.1 m, respectively. The grey and black vectors show UNAVCO processed data. The red triangles and black squares are the GPS and strong-motion stations shown in **g** and **h**. **g**, Comparison of 1-Hz continuous GPS observations[35] (black) and synthetics (red) component-wise cross-correlation coefficients (CC, grey; Methods). **h**, Comparison between synthetic (red) and recorded regional seismograms (black), band-pass filtered between 0.1 Hz and 0.3 Hz, sorted by their azimuth relative to the foreshock epicentre (AZ). CC (grey) from 300-s three-component waveforms. All time series in **g** and **h** are normalized by peak amplitudes (values, top right). EW, east–west; NS, north–south; UD, vertical.

dynamic rupture scenario generates M_w 6.5, in agreement with observations[8,28,29]. Dynamic rupture speed increases from 1.5 km s^{-1} to 2.5 km s^{-1} with distance from the hypocentre, with an average fault-local speed of 2 km s^{-1} (Supplementary Fig. 6). Although a direct comparison with observations is challenged by the medium size and multi-fault conjugate dynamics of the foreshock, the fault-local rupture speed agrees with the rupture velocity inferred in the PSI and other kinematic models (2.4–2.6 km s^{-1})[8]. Local differences of the PSI model include lower

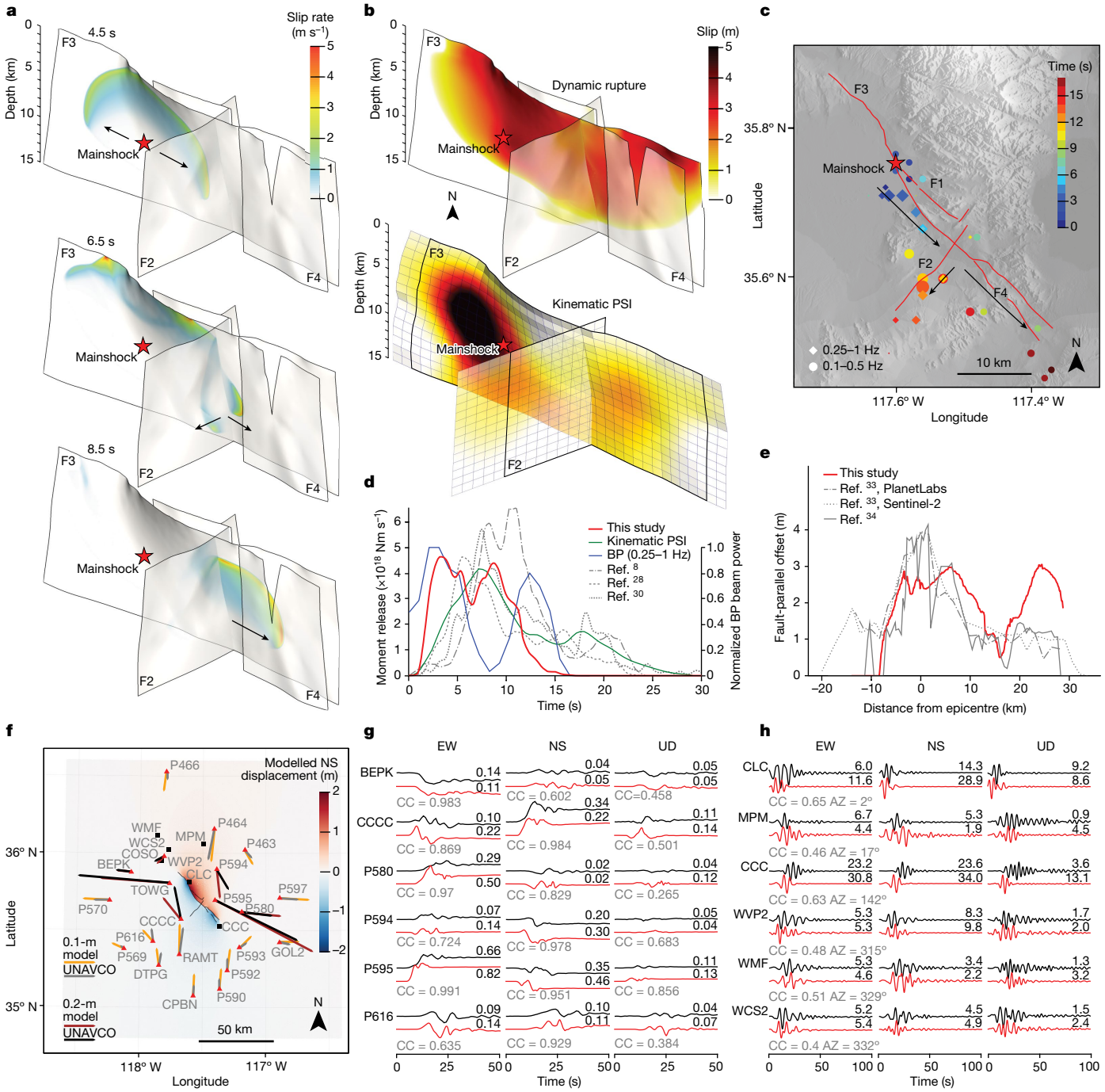

Fig. 3 | Dynamic rupture scenario of the Ridgecrest mainshock and comparison with observations. The details are the same as in Fig. 2. **a**, Snapshots of absolute slip rate (see also Supplementary Video 2). **b**, Fault slip of the dynamic rupture model (top) and kinematic PSI (bottom). **c**, Aftershock-calibrated backprojection (based on 0.1–0.5 Hz and 0.25–1 Hz frequency bands, respectively). **d**, Dynamic rupture moment release rate and backprojection beam power compared with kinematic models. **e**, Fault-parallel surface offsets along F3. **f**, Horizontal (NS) coseismic surface deformation. Synthetic horizontal displacement vectors are scaled by 0.1 m and 0.2 m and the underlying map view shows modelled NS displacements. **g**, Comparison of synthetic (red) and 1-Hz continuous GPS observations[35] (black). **h**, Comparison between synthetic (red) and recorded regional seismograms (black).

kinematic slip at depth on F1 and F2 and a more localized slip patch at shallow depth on F2. The latter is probably owing to the Occam's razor principle implicitly preferring simple, localized slip distributions (Methods).

Our aftershock-calibrated backprojection (Supplementary Table 3 and Methods) of Alaska array data implies orthogonal rupture during the foreshock (Fig. 2c), in agreement with our modelled earthquake dynamics. Backprojection captures an approximately 6-km northwest-propagating rupture on F1 followed by rupture to the southwest tip of F2. From beam power analysis (Fig. 2d), the inferred high-frequency radiators on F1 and F2 appear equally significant. The normalized backprojection beam power resembles the apparent array moment rate of the dynamic rupture model, specifically its two distinct peaks linked to consecutive slip on F1 and F2. In contrast, dominating slip on F2 is characteristic in other published kinematic models (Fig. 2d) and observational moment rates show a weaker early phase than our dynamic model. This may reflect the generally lower sensitivity of kinematic methods to deep slip, especially when overprinted by a

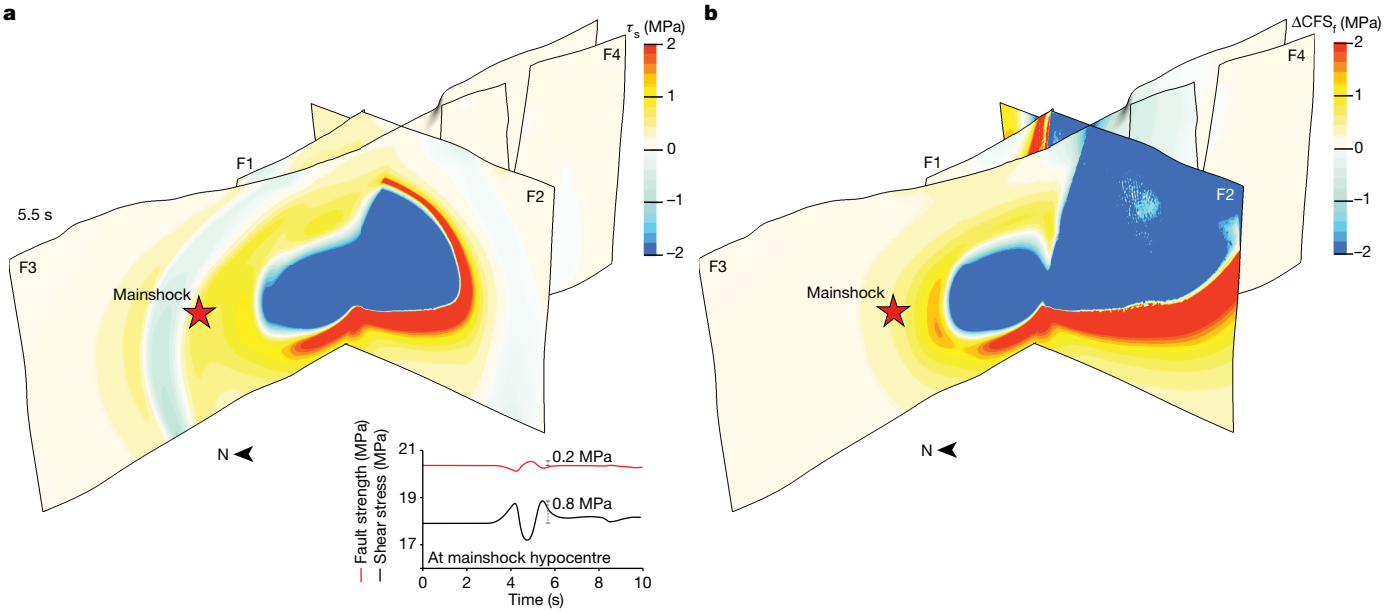

Fig. 4 | Coseismic and postseismic stress changes. a, Along-strike dynamic shear stress perturbation after 5.5 s of foreshock dynamic rupture. Inset: evolution of dynamic shear stress and fault strength during the first 10 s of foreshock dynamic rupture at the mainshock hypocentre (red star). Foreshock dynamic rupture induces an absolute shear stress perturbation of at most approximately 0.8 MPa, while peak normal stress changes of about 0.2 MPa clamp and unclamp F3 at the mainshock hypocentre. **b**, Post-foreshock scalar Coulomb failure stress changes ΔCFS_f, calculated as $\Delta CFS_f = \Delta\tau - f'\Delta\sigma_n$, where $\Delta\tau$ and $\Delta\sigma_n$ are the total shear and normal fault stress change, and $f' = f(1-\gamma) = 0.4$ is the effective friction coefficient. The colour bar is saturated at ±2 MPa.

dominating, shallow rupture. Contrarily, in our dynamic model, rupture along F1 is required to load and trigger rupture on F2.

The spontaneous dynamic rupture scenario reproduces key characteristics of space geodesy, strong-motion, high-rate GPS and teleseismic recordings. The modelled fault-parallel offsets compare well with subpixel satellite image correlation measurements along the surface rupture of F2[33] (Fig. 2e and Supplementary Fig. 7a,b). Also, the modelled static surface deformation is in agreement with geodetic observations from Global Navigation Satellite System and satellite imagery (Fig. 2f), and dominated by large, shallow slip on F2. We observe a striking match (Fig. 2g) between synthetic and observed near-fault 1-Hz continuous GPS data[35]. The synthetics capture the shape and amplitude of characteristic waveform pulses well, such as the first east–west component strong pulse at stations CCCC and P595. Synthetic velocity time series agree with regional strong-motion data (Fig. 2h and Supplementary Fig. 8) and long-period teleseismic recordings (Supplementary Fig. 9a).

Dynamics of the Ridgecrest mainshock

We find that a realistic dynamic rupture scenario of the Ridgecrest mainshock needs to fully account for the stress changes due to the Searles Valley foreshock in addition to the regional complex 3D structure and ambient stress (Supplementary Figs. 10–12 and Methods). Modelling both events in the same dynamic rupture simulation, we find that the foreshock does not dynamically trigger the mainshock. The additional shear stress relative to our assumed fault strength and 3D prestress required to activate F3 at the mainshock hypocentre is 18 MPa peak and about 3 MPa averaged across the numerically determined minimal-sized and smooth critical perturbation area (Supplementary Fig. 13 and Methods). Locally higher fluid pressure reducing effective normal stress, a locally statically weaker fault or combinations of heterogeneities may provide equivalent nucleation mechanisms at lower shear-stress increase.

Figure 3a and Supplementary Video 2 illustrate the modelled complex mainshock earthquake dynamics. During the first 5 s, a crack-like rupture expands bilaterally on F3, then smoothly terminates to the north owing to locally lower prestress and less-optimal fault orientation (Supplementary Fig. 5). The pronounced stress shadow of the M_w 6.4 foreshock (Fig. 4) leads to near-complete termination of southwards rupture in the vicinity of the conjugate F2–F3 intersection, except for decelerated slip at greater depth (at 6.5 s; Fig. 3a). This deep, persistent and 'tunnelling' rupture pulse slowly regrows towards the southeast until the northwest segment of F3 is entirely ruptured at 8.5 s. The conjugate segment F2 is re-activated while the main rupture front passes, aided by dynamic frictional restrengthening during the foreshock pulse-like rupture. Shallow parts of F4 are dynamically unclamped and slip during rupture of F3. Spontaneous dynamic rupture accumulates a continuous slip patch spanning F3 (Fig. 3b), modulated by the combined effects of fault geometry, ambient stress and structural heterogeneities, and foreshock stress shadows. Similarly to the foreshock, the modelled mainshock slip distribution agrees with kinematic models that assume comparable fault geometries within the range of inherent uncertainties, such as our strong-motion PSI model (Fig. 3b). Conjugate fault reactivation is suggested by our PSI, in our low frequency (0.1–0.5 Hz and 0.25–1 Hz) backprojection results (Fig. 3c and Supplementary 14), as well as from joint inversion of InSAR, optical imagery and GPS measurements[10].

Rupture speed increases by about 25% from northwest to southeast and is strongly depth dependent. The average apparent rupture speed is 2.5 km s^{-1} (Supplementary Fig. 6) agreeing with our PSI model (2.1–2.4 km s^{-1}) and backprojection (2.5 km s^{-1}) (Supplementary Fig. 14d). The moment release rate of our dynamic model, beam power evolution in our backprojection and other kinematic models including PSI (Fig. 3d) consistently feature two peaks, which resemble the dynamic delay of F3 rupture when crossing the conjugate intersection with F2 in our model. Our modelled shallow rupture is slower and appears to agree better with data-driven estimates[1,8,28,30], which may be due to less well constrained deeper fault zone geometry and structure.

Our synthetic F3-parallel surface offsets (Fig. 3e) reflect the along-strike dynamic rupture variability and peak close to the epicentre, in overall agreement with satellite images[33]. The physics-based model matches coseismic geodetic observations, such as the orientation of

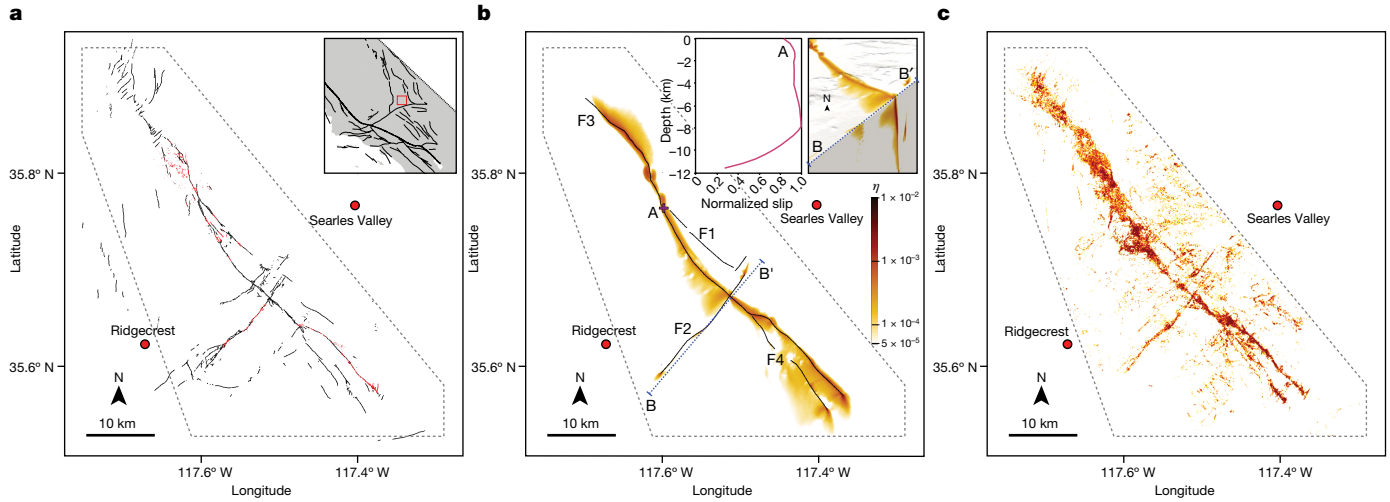

Fig. 5 | Off-fault surface deformation and shallow slip deficit. a, Surface rupture mapping from field observations (black)[41] and high-resolution aerial imagery (red)[42]. Inset: location within the ECSZ. **b**, Modelled off-fault plastic strain, quantified as η (Methods). Insets: depth profile of normalized slip at the epicentre (red cross at A; left) and cut-away view combining a map view and a vertical slice through the flower-like damage zone (accumulated off-fault plastic strain η; right). **c**, Damage proxy map[1] generated from preseismic and postseismic InSAR coherence data.

the observed GPS displacements (Fig. 3f), surprisingly well. Although forward modelling overshoots some static GPS amplitudes, the modelled fault-parallel surface displacements are comparable with satellite imagery (Supplementary Fig. 7c,d). The dynamic model reproduces key characteristics of continuous GPS (Fig. 3g), strong-motion (Fig. 3h and Supplementary Fig. 15) and teleseismic waveforms (Supplementary Fig. 9b). Pulse-like ground motion, with possibly increased damaging potential, was identified in near-fault observations of both earthquakes[36]. We dynamically reproduce such strong impulsive signals at stations CLC, the closest station to the mainshock epicentre, MPM, WVP2, WMF and WCS2 in the northwest extension of rupture on F3, and CCC, close to the southeast tip of rupture on F4 (Fig. 3h), owing to a combination of partially pulse-like rupture, fault reactivation, strong directivity and near-source fling effects.

Conversations between earthquakes

The average dynamic on-fault stress drop is 4 MPa and 5.4 MPa during spontaneous foreshock and mainshock rupture, respectively, and varies with depth and along-strike for all activated faults (Supplementary Fig. 16). This 30%-higher mainshock stress drop directly relates to our dynamic models requiring differences in static pore fluid pressure: the mainshock faults F3 and F4 are governed by an equivalently 30%-lower pore fluid pressure than foreshock faults F1 and F2 (Supplementary Fig. 4c) to achieve realistic levels of fault slip, stress drop and dynamically viable rupture cascading for both events in the same model.

Foreshock dynamic rupture induces an absolute shear stress perturbation of at most approximately 0.8 MPa at the mainshock hypocentre (Fig. 4a). With peak normal stress changes of about 0.2 MPa additionally clamping and unclamping F3 (inset of Fig. 4a), both perturbations are not sufficient to dynamically trigger the mainshock rupture. Although our model suggests that dynamic triggering of the mainshock is mechanically inconceivable, it also shows that the complex foreshock Coulomb stress changes bring the mainshock hypocentral area closer to failure: the mainshock hypocentre of F3 is located within a narrow band experiencing positive Coulomb stress change of up to +0.25 MPa (Fig. 4b and Methods).

The modelled foreshock rupture spontaneously terminates on F1, without reaching the surface and within about 3-km horizontal distance to the F3 mainshock hypocentre. This gap in dynamic slip agrees with the inferred gap in relocated aftershocks following the foreshock[1], which was successively filled by a series of moderate-sized earthquakes[37], including an M_w 5.4 earthquake within 2 km of the mainshock hypocentre. The static Coulomb stress changes of this event, however, were found to be negative at the mainshock hypocentre[11], although not well constrained.

Our models do not include stress changes due to aseismic processes such as postseismic slip and deep fault creep. The shear stress carried by afterslip is potentially considerable, implying interaction of coseismic and postseismic slip and their stresses[12]. We analytically estimate[38] (Methods) a peak shear stress increase of 2.5–4.5 MPa for an average afterslip creep front speed of 3 km in 34 h and our assumed effective normal stress of 20.5 MPa at 8-km hypocentral depth. Seamlessly modelling the full spectrum of slip will be important to capture the interactions between foreshocks, mainshocks and aftershocks[39,40].

The distribution of surface rupture and damage mapped from field and aerial observations[1,41,42] (Fig. 5a,c) align with our prescribed fault geometries and the modelled dynamically induced off-fault yielding (Methods), which accumulates in the vicinity of complexities in fault system geometry (Fig. 5b). The moment contribution of off-fault plastic strain (Methods) in our models is non-negligible, accounting for 3% and 8% of the total seismic moments of the modelled foreshock (M_w 6.45) and mainshock (M_w 7.01), respectively. We observe a shallow slip deficit of up to 20% above 2-km depth (inset in Fig. 5b), which agrees with joint GPS, ground motion and InSAR inversion[12].

We showcase the sensitivity of our physics-based models in four alternative scenarios including: mainshock dynamic rupture models (1) not accounting for the foreshock stress changes (Supplementary Fig. 10); (2) in addition, not incorporating the long-term Coulomb failure stress changes (ΔCFS) (Supplementary Fig. 11); and combined foreshock and mainshock models (3) omitting the long-term ΔCFS (Supplementary Figs. 12 and 17); and (4) loaded with an alternative community ambient stress model (Supplementary Fig. 18). Local rupture dynamics, as well as the dynamic activation of segments of the sequence, change when key modelling ingredients are altered (Supplementary Fig. 19 and Methods). In particular, not incorporating the long-term ΔCFS prevents correctly capturing the conjugate, partially surface-breaking character of the foreshock rupture.

Using a rate-and-state friction law with strong velocity weakening facilitates the concept of statically strong and dynamically weak faults. If we assumed higher dynamic strength, our relative fault prestress R would decrease (equation (9) and Methods). The dynamic rupture

cascading potential may then be restored by local stress, strength or pore fluid pressure changes reflecting natural fault zone heterogeneity. For example, concentrating relative prestress at depth would allow us to approximate the expected effects of deep aseismic creep[17,21].

By assimilating models and data of structural characteristics, tectonic stress, seismogenic depth and long-term stress changes, we constrain multi-fault dynamic rupture scenarios that self-consistently intertwine the 2019 Searles Valley and Ridgecrest multi-fault earthquake dynamics, and unify seismic, geodetic and geological observations. The match with observations, achieved across scales, is remarkable, given that we do not solve an inverse problem. Including small-scale heterogeneities may improve physics-based synthetics at higher frequencies[43]. Our approach demonstrates that data-driven and physics-based modelling can be combined to shed light on the underlying physics of cascading multi-fault earthquake sequences. Our results imply that the long-term and short-term as well as the dynamic and static fault system interaction are crucial for future seismic hazard assessment of active multi-fault systems.

Online content

Any methods, additional references, Nature Portfolio reporting summaries, source data, extended data, supplementary information, acknowledgements, peer review information; details of author contributions and competing interests; and statements of data and code availability are available at https://doi.org/10.1038/s41586-023-05985-x.

1. Ross, Z. E. et al. Hierarchical interlocked orthogonal faulting in the 2019 Ridgecrest earthquake sequence. *Science* **366**, 346–351 (2019).
2. Hauksson, E., Jones, L. M., Hutton, K. & Eberhart-Phillips, D. The 1992 Landers earthquake sequence: seismological observations. *J. Geophys. Res. Solid Earth* **98**, 19835–19858 (1993).
3. Hamling, I. J. et al. Complex multifault rupture during the 2016 M_w 7.8 Kaikoura earthquake, New Zealand. *Science* **356**, eaam7194 (2017).
4. DuRoss, C. B. et al. Surface displacement distributions for the July 2019 Ridgecrest, California, earthquake ruptures. *Bull. Seismol. Soc. Am.* **110**, 1400–1418 (2020).
5. Zeng, Y. & Shen, Z. A fault-based model for crustal deformation, fault slip rates, and off-fault strain rate in California. *Bull. Seismol. Soc. Am.* **106**, 766–784 (2016).
6. Fukuyama, E. Dynamic faulting on a conjugate fault system detected by near-fault tilt measurements. *Earth Planet. Space* **67**, 38 (2015).
7. Kato, A., Sakai, S., Matsumoto, S. & Iio, Y. Conjugate faulting and structural complexity on the young fault system associated with the 2000 Tottori earthquake. *Commun. Earth. Environ.* **2**, 13 (2021).
8. Chen, K. et al. Cascading and pulse-like ruptures during the 2019 Ridgecrest earthquakes in the Eastern California Shear Zone. *Nat. Commun.* **11**, 22 (2020).
9. Shi, Q. & Wei, S. Highly heterogeneous pore fluid pressure enabled rupture of orthogonal faults during the 2019 Ridgecrest M_w7.0 earthquake. *Geophys. Res. Lett.* **47**, e2020GL089827 (2020).
10. Magen, Y., Ziv, A., Inbal, A., Baer, G. & Hollingsworth, J. Fault rerupture during the July 2019 Ridgecrest earthquake pair from joint slip inversion of InSAR, optical imagery, and GPS. *Bull. Seismol. Soc. Am.* **110**, 1627–1643 (2020).
11. Jin, Z. & Fialko, Y. Finite slip models of the 2019 Ridgecrest earthquake sequence constrained by space geodetic data and aftershock locations. *Bull. Seismol. Soc. Am.* **110**, 1660–1679 (2020).
12. Qiu, Q., Barbot, S., Wang, T. & Wei, S. Slip complementarity and triggering between the foreshock, mainshock, and afterslip of the 2019 Ridgecrest rupture sequence. *Bull. Seismol. Soc. Am.* **110**, 1701–1715 (2020).
13. Shelly, D. R. A high resolution seismic catalog for the initial 2019 Ridgecrest earthquake sequence: foreshocks, aftershocks, and faulting complexity. *Seismol. Res. Lett.* **91**, 1971–1978 (2020).
14. Cheng, Y. & Ben-Zion, Y. Variations of earthquake properties before, during, and after the 2019 *M*7.1 Ridgecrest, CA, earthquake. *Geophys. Res. Lett.* **47**, e2020GL089650 (2020).
15. Wang, K., Dreger, D. S., Tinti, E., Bürgmann, R. & Taira, T. Rupture process of the 2019 Ridgecrest, California M_w 6.4 foreshock and M_w 7.1 earthquake constrained by seismic and geodetic data. *Bull. Seismol. Soc. Am.* **110**, 1603–1626 (2020).
16. Lachenbruch, A. H. & Sass, J. Heat flow and energetics of the San Andreas Fault zone. *J. Geophys. Res. Solid Earth* **85**, 6185–6222 (1980).
17. Ulrich, T., Gabriel, A.-A., Ampuero, J.-P. & Xu, W. Dynamic viability of the 2016 M_w 7.8 Kaikoura earthquake cascade on weak crustal faults. *Nat. Commun.* **10**, 1213 (2019).
18. Li, B. & Ghosh, A. in *The Chile-2015 (Illapel) Earthquake and Tsunami* (eds Braitenberg, C. & Rabinovich, A. B.) 33–43 (Springer, 2017).
19. Hallo, M. & Gallovič, F. Bayesian self-adapting fault slip inversion with Green's functions uncertainty and application on the 2016 M_w7.1 Kumamoto earthquake. *J. Geophys. Res. Solid Earth* **125**, e2019JB018703 (2020).
20. Carena, S. & Suppe, J. Three-dimensional imaging of active structures using earthquake aftershocks: the Northridge thrust, California. *J. Geol. Soc.* **24**, 887–904 (2002).
21. Liang, C., Ampuero, J.-P. & Pino Muñoz, D. Deep ductile shear zone facilitates near-orthogonal strike-slip faulting in a thin brittle lithosphere. *Geophys. Res. Lett.* **48**, e2020GL090744 (2021).
22. Lee, E.-J. et al. Full-3-D tomography for crustal structure in Southern California based on the scattering-integral and the adjoint-wavefield methods. *J. Geophys. Res. Solid Earth* **119**, 6421–6451 (2014).
23. Yang, W. & Hauksson, E. The tectonic crustal stress field and style of faulting along the Pacific North America Plate boundary in Southern California. *Geophys. J. Int.* **194**, 100–117 (2013).
24. Verdecchia, A. & Carena, S. Coulomb stress evolution in a diffuse plate boundary: 1400 years of earthquakes in eastern California and western Nevada, USA. *Tectonics* **35**, 1793–1811 (2016).
25. Copley, A. The strength of earthquake-generating faults. *J. Geol. Soc.* **175**, 1–12 (2017).
26. Di Toro, G. et al. Fault lubrication during earthquakes. *Nature* **471**, 494–498 (2011).
27. *Southern California Earthquake Data Center* (SCEDC, 2013); https://scedc.caltech.edu.
28. Goldberg, D. E. et al. Complex rupture of an immature fault zone: a simultaneous kinematic model of the 2019 Ridgecrest, CA earthquakes. *Geophys. Res. Lett.* **47**, e2019GL086382 (2020).
29. Liu, M., Zhang, M., Zhu, W., Ellsworth, W. L. & Li, H. Rapid characterization of the July 2019 Ridgecrest, California, earthquake sequence from raw seismic data using machine-learning phase picker. *Geophys. Res. Lett.* **47**, e2019GL086189 (2020).
30. Liu, C., Lay, T., Brodsky, E. E., Dascher-Cousineau, K. & Xiong, X. Coseismic rupture process of the large 2019 Ridgecrest earthquakes from joint inversion of geodetic and seismological observations. *Geophys. Res. Lett.* **46**, 11820–11829 (2019).
31. Lozos, J. C. & Harris, R. A. Dynamic rupture simulations of the *M*6.4 and *M*7.1 July 2019 Ridgecrest, California, earthquakes. *Geophys. Res. Lett.* **47**, e2019GL086020 (2020).
32. Cortez, J. T. et al. On the rupture propagation of the 2019 *M*6.4 Searles Valley, California, earthquake, and the lack of immediate triggering of the *M*7.1 Ridgecrest earthquake. *Geophys. Res. Lett.* **48**, e2020GL090659 (2021).
33. Milliner, C. & Donnellan, A. Using daily observations from Planet Labs satellite imagery to separate the surface deformation between the 4 July M_w 6.4 foreshock and 5 July M_w 7.1 mainshock during the 2019 Ridgecrest earthquake sequence. *Seismol. Res. Lett.* **91**, 1986–1997 (2020).
34. Gabriel, A.-A., Ampuero, J.-P., Dalguer, L. A. & Mai, P. M. The transition of dynamic rupture styles in elastic media under velocity-weakening friction. *J. Geophys. Res.* **117**, B09311 (2012).
35. Melgar, D. et al. Real-time high-rate GNSS displacements: performance demonstration during the 2019 Ridgecrest, California, earthquakes. *Seismol. Res. Lett.* **91**, 1943–1951 (2019).
36. Baltzopoulos, G., Luzi, L. & Iervolino, I. Analysis of near-source ground motion from the 2019 Ridgecrest earthquake sequence. *Bull. Seismol. Soc. Am.* **110**, 1495–1505 (2020).
37. Toda, S. & Stein, R. S. Long- and short-term stress interaction of the 2019 Ridgecrest sequence and Coulomb-based earthquake forecasts. *Bull. Seismol. Soc. Am.* **110**, 1765–1780 (2020).
38. Garagash, D. I. Fracture mechanics of rate-and-state faults and fluid injection induced slip. *Phil. Trans. R. Soc. A.* **379**, 20200129 (2021).
39. Yue, H. et al. The 2019 Ridgecrest, California earthquake sequence: evolution of seismic and aseismic slip on an orthogonal fault system. *Earth Planet Sci. Lett.* **570**, 117066 (2021).
40. Premus, J., Gallovič, F. & Ampuero, J.-P. Bridging time scales of faulting: from coseismic to postseismic slip of the M_w 6.0 2014 South Napa, California earthquake. *Sci. Adv.* **8**, eabq2536 (2022).
41. Ponti, D. J. et al. Documentation of surface fault rupture and ground-deformation features produced by the 4 and 5 July 2019 M_w 6.4 and M_w 7.1 Ridgecrest earthquake sequence. *Seismol. Res. Lett.* **91**, 2942–2959 (2020).
42. Rodriguez Padilla, A. M. et al. Near-field high-resolution maps of the Ridgecrest earthquakes from aerial imagery. *Seismol. Res. Lett.* **93**, 494–499 (2021).
43. Taufiqurrahman, T., Gabriel, A.-A., Ulrich, T., Valentova, L. & Gallovič, F. Broadband dynamic rupture modeling with fractal fault roughness, frictional heterogeneity, viscoelasticity and topography: the 2016 M_w 6.2 Amatrice, Italy earthquake. *Geophys. Res. Lett.* **31**, e2022GL098872 (2022).
44. Antoine, S. L. et al. Diffuse deformation and surface faulting distribution from submetric image correlation along the 2019 Ridgecrest, California, ruptures. *Bull. Seismol. Soc. Am.* **111**, 2275–2302 (2021).

Methods

Numerical method

We solve the nonlinearly coupled spontaneous dynamic rupture and seismic wave propagation problem with high-order accuracy in space and time using the open-source software SeisSol (https://github.com/SeisSol/SeisSol). SeisSol uses the arbitrary high-order accurate derivative discontinuous Galerkin method[45] and end-to-end optimization for high-performance-computing infrastructure[46–50]. SeisSol employs fully non-uniform unstructured tetrahedral meshes that statically adapt to geometrically complex 3D geological structures, such as non-planar mutually intersecting faults and topography. SeisSol is verified in a wide range of community benchmarks[51] by the Southern California Earthquake Center (SCEC) and US Geological Survey Dynamic Rupture Code Verification project[52,53].

We link the foreshock and mainshock dynamic rupture earthquake models in the same simulation to account for the dynamic and static stress changes of the foreshock rupture in our scenario of the mainshock. Owing to the lack of intermediate, spontaneous dynamic triggering of the mainshock in our models, we quantify the required additional prestress to initiate the mainshock at the mainshock hypocentre at 100 s after initiating the foreshock. This time span ensures that all transient seismic waves emitted during the foreshock have left the model domain.

Fault geometry

We use a surface fitting technique[20] to generate a 3D geometric model independently of a priori structural interpretation of the conjugate fault network that may have ruptured during the 2019 Ridgecrest sequence (Supplementary Fig. 1a). Our fault model is based on relocated earthquake hypocentre locations[1] combined with earthquake focal mechanisms[25] and fault surface traces. We map fault surface traces from a combination of InSAR data[54], public satellite imagery (earth.google.com/web/) where pre- and post-earthquake images can be compared, private satellite imagery[55] and digital elevation models (apps.nationalmap.gov/viewer/). To map the foreshock faults, we use only hypocentres and focal mechanisms of those events that occurred in-between the foreshock and mainshock. For the mainshock faults, we use only aftershocks that occurred during the first 48 h after the mainshock. Surface traces are set as 3D fixed constraints. We use the software SKUA-GOCAD as the modelling environment. The model is composed of four geometrically complex fault segments (Fig. 1 and Supplementary Fig. 1a): three northwest–southeast-trending faults (F1, F3 and F4) and a conjugate northeast–southwest-trending segment (F2). The largest fault, F3, is about 45-km long (Supplementary Fig. 1a). Its dip varies from about 80° southwest in its northern part to about 70° northeast south of the mainshock hypocentre, which results in a helical fault geometry[21,56]. F1, an approximately 15-km-long segment parallel to F3, and F2, an approximately 20-km-long conjugate segment, are the main structures dynamically activated during the foreshock. F4 is an approximately 15-km-long branch in the southwest of F3, and F2, F3 and F4 all slip dynamically during the mainshock. Our constructed faults align with the updated SCEC Community Fault Model (version 5.3, https://zenodo.org/record/5899364; Supplementary Fig. 1b), including fault representations for the Ridgecrest earthquake sequence[57]. We omit secondary features, such as smaller orthogonal faults that appear as shallow lineations in seismicity[1] and space geodesy[58] (Supplementary Fig. 1). Our modelled distributed off-fault plastic strain, however, aligns with regions of observed off-fault damage (Fig. 5).

Fault friction

We adopt a strong velocity-weakening rate-and-state friction law[53,59] that allows the reproduction of the severe reduction of coseismic friction observed in laboratory experiments at high slip rates[27]. With this friction law, our fault system is operating at low average shear stress (Supplementary Fig. 5) while dynamically yielding reasonable levels of fault slip and stress drop. This friction law also facilitates rupture cascading across the conjugate fault network and coseismic complexity such as rupture pulse-to-crack transition and coseismic restrengthening[34,60,61].

In a rate-and-state framework, frictional fault strength depends on the state of the fault surface as well as the current slip rate[62,63]. The strength of each fault is assumed to be proportionate to the magnitude of shear traction τ

$$\tau = f(V, \Psi)\sigma_n', \tag{1}$$

where f is the effective friction coefficient, V is slip rate, Ψ is the state variable and σ_n' is the effective normal stress. τ and V are parallel and satisfy $\tau V = V\tau$. The instantaneous friction coefficient f depends on V and Ψ and is calculated as

$$f(V, \Psi) = a \sinh^{-1}\left(\frac{V}{2V_0}\exp\left(\frac{\Psi}{a}\right)\right), \tag{2}$$

where a is the direct-effect parameter and V_0 is the reference velocity. The evolution of Ψ is governed by

$$\frac{d\Psi}{dt} = -\frac{V}{L}(\Psi - \Psi_{ss}(V)), \tag{3}$$

where L is a characteristic slip distance of state evolution, t is time and Ψ_{ss} is the steady-state value of the state variable and is given by

$$\Psi_{ss} = a \ln\left(\frac{2V_0}{V}\sinh\left(\frac{f_{ss}(V)}{a}\right)\right). \tag{4}$$

The steady-state friction coefficient f_{ss} is

$$f_{ss}(V) = f_w + \frac{f_{LV}(V) - f_w}{(1 + (V/V_w)^8)^{1/8}}, \tag{5}$$

where f_{LV} is the low-velocity friction coefficient, which depends on f_0, defined as the steady-state low-velocity friction coefficient at V_0, and is given by

$$f_{LV}(V) = f_0 - (b - a)\ln\frac{V}{V_0}. \tag{6}$$

All frictional parameters we prescribe are listed in Supplementary Table 2. We note that we do not directly prescribe the maximum static friction coefficient (μ_s), which dynamically varies across the fault system and may exceed f_0.

Supplementary Fig. 4a shows the depth-dependent direct-effect parameter a and constant evolution-effect parameter b. The parameter a linearly increases to 4 km depth, such that the fault frictional behaviour transitions from velocity weakening to velocity strengthening at 1.8-km depth. The assumed increase of $a - b$ at shallow depth is motivated by (1) direct shear and triaxial experiments[64] showing temperature dependence of this parameter, (2) models reproducing the variability of shallow creep behaviour in both postseismic and interseismic periods[65] and (3) previous dynamic rupture modelling[66].

Prestress

We construct an ambient 3D heterogeneous prestress combining observations with simple theoretical analysis and community models.

2D community stress model. We adapt stress as a normalized zero-trace tensor S_{ij} from the 2D community stress model YHSM-2013[23], provided by the SCEC (https://scec.org/research/csm/). The YHSM-2013

community stress model is based on damped stress inversion from high-quality Southern California Seismic Network earthquake focal mechanisms from 1981 to 2010[23] and provides the time-averaged regional lateral variation of the maximum horizontal compressional stress SH_{max} and the stress shape ratio ν in our model domain (Supplementary Fig. 2). Stress orientations vary on a range of length scales. Similar to other community stress models, YHSM-2013 can resolve the regional larger-scale heterogeneity (5–10 km) of the ambient stress state, but lacks resolution for local stress heterogeneity at smaller scales. We use 0.02° (about 2 km) interpolated YHSM-2013 data. Using inverse multiquadratic radial basis function interpolation and a Gaussian filter with a standard deviation for the Gaussian kernel of $\sigma = 2$, we smooth any sharp transitions within the stress model.

The stress shape ratio ν describes different faulting mechanisms depending on the eigenvalues (S_1, S_2 and S_3; ordered from most compressional to most tensional) of the ambient stress tensor S_{ij}, with

$$\nu = \frac{S_2 - S_3}{S_1 - S_3}. \quad (7)$$

When S_2 is vertical, as inferred for the Ridgecrest earthquake region[23], $\nu < 0.5$ characterizes a transpressional regime, $\nu = 0.5$ characterizes a pure strike-slip regime and $\nu > 0.5$ characterizes a transtensional regime.

Relative fault prestress. We use a systematic approach that allows us to constrain the orientation of all principal stresses and the magnitudes of deviatoric stresses[17], and that extends the Mohr–Coulomb theory of frictional failure with dynamic parameters while reducing the large parameter space common in dynamic rupture modelling[67]. We assume that the ambient prestress is 3D heterogeneous and always Andersonian[68], that is, one principal stress component (S_2) is vertical. We then combine this with the relative fault prestress R (ref. 69), which is the ratio of the potential stress drop to the full breakdown strength drop. R is defined as

$$R = \frac{\tau - \mu_d \sigma'_n}{(\mu_s - \mu_d)\sigma'_n}. \quad (8)$$

$R_0 = 1$ indicates a critical prestress level on all optimally oriented faults. To compute R, we assume $\mu_d \approx f_w$, with μ_d being a constant dynamic friction coefficient, as we observe that the fully weakened friction f_w is typically reached in our simulations, and $\mu_s \approx f_0$ as a conservative assumption, since the dynamically reached maximum friction coefficient μ_s varies along the fault and often exceeds f_0, thus

$$R \approx \frac{\tau - f_w \sigma'_n}{(f_0 - f_w)\sigma'_n}. \quad (9)$$

We note that both approximations may result in locally slightly smaller R than the one we report in Fig. 1c for the preferred rupture models and in Supplementary Fig. 17 for alternative scenarios not accounting for the long-term ΔCFS.

The absolute magnitude of all principal stresses can then be fully described by (1) the maximum relative fault prestress R_0 of virtual fault segments optimally oriented in the stress field, which constrains the smallest and largest principal stress components, (2) the pore fluid pressure ratio γ, describing overpressurized fault zone fluids[70], and modulating effective normal stress σ'_n gradients[71], with a hydrostatic state defined as $\gamma = \rho_{water}/\rho = 0.37$, with ρ being rock density (2,700 kg m^{-3}) and ρ_{water} being the density of water, and higher values of γ corresponding to overpressurized pore fluids, and (3) the stress shape ratio ν.

We compute an ambient depth-dependent prestress tensor, b_{ij}, constrained by SH_{max}, ν, R_0 and γ, by assuming the vertical stress as

$$\sigma_{zz} = \int_0^z \rho(x,y,z')g \, dz' = g\int_0^z \rho(x,y,z') \, dz' = \overline{\rho}(x,y,z)gz, \quad (10)$$

with $\overline{\rho}(x,y,z) = \frac{1}{z}\int_0^z \rho(x,y,z') \, dz'$ being the density of the 3D heterogeneous overburden (based on the velocity model CVM-S4.26 used here[22]), and $g = 9.8$ m s^{-2} being the gravitational acceleration. Fluid pressure is then assumed to be proportional to vertical stress σ_{zz} as $P_f = \gamma\sigma_{zz}$ and the effective vertical stress is $\sigma'_{zz} = (1-\gamma)\sigma_{zz}$.

Long-term Coulomb failure stress changes. We add to the ambient depth-dependent prestress tensor b_{ij}, defined in the previous section, the contribution c_{ij} of coseismic and postseismic Coulomb failure stress changes (ΔCFS) caused by major historical earthquakes ($M_w \geq 7$) that have occurred in the ECSZ during the past roughly 1,400 years[24], as well as by recent events of smaller magnitude. This new static stress change model (Supplementary Fig. 20 and Supplementary Table 1) accounts for eight additional historical and recent events compared with earlier published versions[24].

Figure 1b and Supplementary Fig. 21a show the associated changes in Coulomb failure stress ΔCFS at 5-km depth, assuming a northwest-striking fault plane with strike 318°, dip 88° and rake −170°. Before the start of the 2019 Ridgecrest sequence, the computed ΔCFS is about 0.8 MPa at the location of the foreshock hypocentre, but only about 0.4 MPa at the mainshock hypocentre. We include the two largest events (M_w 5.8 and M_w 4.9) of the 1995 Ridgecrest earthquake sequence, which reduces prestress near the mainshock hypocentre (Fig. 1d). We isolate the contribution of the two 1995 earthquakes by calculating ΔCFS due to only these two events and ΔCFS due to all others (Supplementary Fig. 21). Both occurred in close proximity to the fault system without causing clear surface rupture[72]. The effects of the 1995 M_w 5.8 and M_w 4.9 events are overall local but shadow the hypocentral area of the mainshock, potentially contributing to the delayed triggering. Including previous events in particular on the Garlock Fault, leads to positive Coulomb failure stress changes in the foreshock hypocentral area.

We note that we take into account both coseismic and postseismic stress changes due to viscoelastic relaxation of the lower crust and upper mantle, which are thought to play an important role at timescales longer than five years[73]. Also, we reiterate that we do not calculate ΔCFS on an a priori-assumed planar fault geometry, but use a full tensor, which allows us to account for the complexity of the conjugate fault network when resolving on-fault stress changes.

Combined 3D heterogeneous prestress for dynamic rupture modelling. The full prestress tensor s_{ij} used in our dynamic rupture models is obtained by combining the ambient prestress tensor b_{ij} and the pre-Ridgecrest long-term stress change tensor c_{ij}. In addition, we apply a depth-modulation function $\Omega(z)$ (Supplementary Fig. 4b), which smoothly tapers deviatoric stresses below the spatially varying seismogenic depth z_{seis} as:

$$s_{ij}(x,y,z) = \Omega(z)(b_{ij}(x,y,z)) + c_{ij}(x,y,z)) + (1-\Omega(z))\sigma'_{zz}(x,y,z)\delta_{ij}, \quad (11)$$

with z_{seis} constrained by aftershock locations (Supplementary Fig. 3) and δ_{ij} being the Kronecker delta. Additional modulation of the depth dependence of R_0 would allow to account for potential stress concentrations at the bottom of the seismogenic zone induced by deep creep[17,21]. However, the shape and depth of such stress concentration would be difficult to constrain for our complex fault system.

By performing a few dynamic rupture experiments, we find optimal values of γ and R_0, constrained by the mechanic viability of rupture to cascade along the fault network with realistic amounts of fault slip and stress drop. An approximation of the order of magnitude of the

expected dynamic stress drop is $R_0(1-\gamma)\sigma_{zz}(f_0-f_w)$, with $f_0 = 0.6 \approx \mu_s$ the static friction coefficient and $f_w = 0.1 \approx \mu_d$ the fully weakened friction, which demonstrates dynamic trade-offs between R_0 and γ (ref. 17).

We find that a prescribed $R_0 = 0.8$, as the relative prestress of an optimal fault in the complex stress field s_{ij}, is a large enough value to allow for sustained foreshock and mainshock rupture along the conjugate fault system, but small enough to reproduce realistic fault slip and stress drop. For the foreshock, we find that a fluid pressure ratio of $\gamma = 0.83$, well below lithostatic but above hydrostatic, produces spontaneous rupture of both F1 and F2 with an amount of fault slip consistent with inversion studies[8,28]. In comparison, a mainshock dynamic rupture simulation based on the same γ fails to dynamically rupture the southern parts of F3 and F4. A higher stress drop is needed to sustain rupture beyond the conjugate F2–F3 intersection. We find that reducing fluid pressure by 30% and assuming $\gamma = 0.77$ on F3 and F4, thus allowing for 30%-higher potential stress drop than on F1 and F2, allows spontaneous rupture of the southern parts of F3 and F4, well aligned with observations.

Rupture nucleation

In dynamic rupture models, only a small portion, the critical nucleation zone[74], of the fault needs to reach failure to nucleate a rupture while faults can be prestressed well below critical (Supplementary Fig. 5) and yet break spontaneously. Dynamic rupture simulations typically use prescribed nucleation procedures. Three-dimensional earthquake cycle simulations that incorporate spontaneous (aseismic) nucleation and dynamic rupture exist[75–78], but are methodologically and computationally challenging at the same level of combined geometrical, frictional and structural complexity[79,80].

Several techniques for nucleating dynamic earthquake ruptures exist, including locally either elevated shear stress, low (effective) static frictional strength or time-weakening forced rupture[81–84]. We carefully follow established modelling best practices[53,85], using a nucleation patch smoothly varying in space and time and acting across a minimal-sized perturbation area, avoiding artefacts and initiating self-sustained spontaneous rupture with minimal perturbation determined in several trial dynamic rupture simulations. In both the foreshock and mainshock scenarios, spontaneous dynamic rupture is initiated by progressively increasing on-fault shear traction in a spherical volume of radius $r_{nuc} = 3.5$ km centred at their respective hypocentres (Supplementary Table 4). The nucleation overstress $\Delta\tau(r, t)$ is given as:

$$\Delta\tau(r,t) = \tau_{nuc} F(r) G(t), \tag{12}$$

with τ_{nuc} the peak value of the overstress and r the radius from the hypocentre. $F(r)$ defines the shape of the overstress perturbation:

$$F(r) = \begin{cases} \frac{1}{2}\sum_{n=1}^{2} \exp\left[-\frac{1}{2}\left(\frac{r}{r_{crit}(n)}\right)^2\right] & r < r_{nuc} \\ 0 & r \geq r_{nuc} \end{cases} \tag{13}$$

$r_{crit}(n=1)$ and $r_{crit}(n=2)$ are set to 0.4 km and 1.6 km, respectively. For both events, we use $\tau_{nuc} = 18$ MPa, which results in an average nucleation stress of about 3 MPa over the circular nucleation area (Supplementary Fig. 13). $G(t)$ is a smoothed step function given as:

$$G(t) = \begin{cases} \exp\left[\frac{(t-T_{nuc})^2}{t(t-2T_{nuc})}\right] & 0 < t < T_{nuc} \\ 1 & t \geq T_{nuc} \end{cases} \tag{14}$$

with $T_{nuc} = 1$ s.

Analytical interpretation of the dynamically required mainshock nucleation stress

We can interpret the additional shear stress required to activate F3 in our dynamic rupture model using an analytical estimate of the shear stress increase carried by afterslip[38], implying interaction of coseismic and postseismic slip and their stresses[12]. We adapt the analytical 1D estimate of the peak shear stress to normal stress ratio f_p carried by transient afterslip (equation 2.20 of ref. 38) as

$$f_p \approx f_0 + a\ln\frac{v_r/V_0}{\kappa_0\, g(v_r/c_S)}, \tag{15}$$

where f_0 is the initial fault stress ratio at the ambient fault sliding velocity V_0, the constant near-field prefactor $\kappa_0 \approx 1$ and the universal function[86] $g(v_r/c_S) \approx 1$ for aseismic fronts, v_r is the speed of the transient (afterslip) front, $v_0 = \mu V_0/(b\sigma_n)$ is a characteristic rupture velocity embodying the dependence on the fault ambient conditions and c_s is the S wave speed. Assuming v_r to correspond to approximately 3 km in 34 h (ref. 1), $a = 0.01$ and $b = 0.014$ yields a peak shear stress perturbation at the transient front of 2.5–4.5 MPa for ambient fault slip rates $V_0 = 10^{-12} \ldots 10^{-16}$ m s^{-1}.

Sensitivity of the dynamic rupture models

We analyse the sensitivity of the modelled foreshock and mainshock rupture dynamics to key modelling ingredients including the chosen ambient stress set-up and the 3D long-term stress changes. We observe high sensitivity of foreshock rupture dynamics to regional initial conditions, including its simultaneous conjugate rupture, partial surface rupture and lack of coseismic mainshock triggering. We observe high sensitivity of mainshock rupture dynamics to foreshock slip distributions on F1 and F2, for example, with respect to the mainshock's ability to dynamically overcome the geometric and stress barrier posed by the conjugate F2–F3 fault intersection and activate the southern segment of F3.

Our dynamic rupture scenario of the Ridgecrest mainshock fully accounts for the stress changes due to the Searles Valley foreshock in addition to long-term Coulomb failure stress changes ΔCFS. We demonstrate here the effects of (1) not incorporating the foreshock stress changes in an alternative mainshock rupture dynamics simulation, shown in Supplementary Fig. 10 and Supplementary Video 3, and of (2) omitting both foreshock stresses and ΔCFS in alternative mainshock rupture dynamics simulation (Supplementary Fig. 11 and Supplementary Video 4). In both cases, mainshock rupture dynamics are less complex than in the preferred model (Supplementary Fig. 22). In the mainshock model without the foreshock stress changes, spontaneously accumulating fault slip is overall larger than in the preferred mainshock model, especially on F3 near the conjugate F2–F3 intersection (Supplementary Fig. 19a). Unlike the preferred model, this scenario features no rupture delay at this intersection. We also see more shallow slip on F2 and F4 and more slip at shallow depth after the F2–F3 intersection. In the alternative mainshock simulation omitting additionally long-term ΔCFS, fault slip is overall lower and specifically reduced at shallow depth (Supplementary Fig. 19b). We observe less slip to the south of F3, no more slip on F4 and reduced slip on F2. Differences in slip to the south are probably linked to the 1453 M_w 7.7 event on the Garlock Fault[24]. Rupture duration is here about 2 s shorter, owing to the lack of dynamic triggering of F4.

In the alternative combined dynamic rupture models 3 of foreshock and mainshock presented in Supplementary Figs. 12 and 17, and Supplementary Videos 5 and 6, we do not incorporate the pre-Ridgecrest long-term 3D stress changes ΔCFS. In this way, we evidence the non-negligible effects of ΔCFS from previous important earthquakes on foreshock and mainshock rupture dynamics. Supplementary Fig. 12 shows the foreshock scenario, which lacks pronounced rupture on F2 (Supplementary Fig. 19c). Differences in the mainshock slip distribution

include non-rupture of F4, similar to model 2. Slip in the southern F3 region is larger than in model 2 but still reduced with respect to the reference model and not sufficient to dynamically trigger the F4 segment (Supplementary Fig. 19d). Differences in the relative prestress ratio R on all faults highlight the effect of long-term ΔCFS on the relative strength of F2 and on the mainshock hypocentral region at F3 (Supplementary Fig. 17).

Lastly, we analyse the sensitivity to the ambient background stress model by implementing the 3D stress inversion model FM3D[87] instead of YHSM-2013[23]. YHSM-2013 is a 2D model, which has higher lateral resolution in the Ridgecrest region. The alternative combined dynamic rupture models 4 of foreshock and mainshock with the same long-term ΔCFS are shown in Supplementary Fig. 18 and Supplementary Videos 7 and 8. In the FM3D foreshock scenario, both F1 and F2 are ruptured with a higher slip magnitude on F2 compared with the reference scenario (Supplementary Fig. 19e). In the FM3D mainshock scenario, dynamic rupture on F3 terminates at the conjugate intersection with F2, highlighting the sensitivity of a mechanically viable realistic mainshock scenario to the foreshock rupture dynamics and especially to the rupture extent on F2 (Supplementary Fig. 19f).

Computational mesh and model resolution

The model domain used to jointly simulate both events accounts for high-resolution topography and is spatially discretized in an unstructured tetrahedral mesh of 27,264,253 million tetrahedral elements. We retrieved topography data from the Shuttle Radar Topography Mission[88]) using the SRTM.py Python package https://github.com/tkrajina/srtm.py. The spatially adaptive mesh resolution is set to an element edge length of h = 75 m close to all faults and gradually coarsened away from the fault surfaces. The mesh is also refined near topography, and set to h = 500 m element edge lengths at the free surface. We use the WGS84/UTM Mercator 11S projection.

Simulating 200 s of physical simulation time on this computational mesh using high-order basis functions of polynomial order p = 4, leading to a fifth-order space–time accurate numerical scheme for wave propagation, typically requires about 19.5 h on 250 × 48 Skylake cores of the SuperMUC-NG supercomputer (Leibniz Supercomputing Center). Our chosen h, p resolution resolves the seismic wavefield up to at least 2 Hz in the near-source region. Each dynamic rupture element face consists of $(p + 2)^2$ Gauss integration points, enabling subelemental resolution of rupture dynamics[89]. The size of the area behind the rupture front in which shear stress decreases from its static to its dynamic value is the process zone width. In the dynamic rupture models presented, we measure the median process zone width as 6.1 km, whereas for 95% of the ruptured fault elements it is larger than 515 m, which is well resolved by our chosen discretization.

3D velocity model and viscoelastic attenuation

We embed all faults in the SCEC 3D velocity model CVM-S4.26 (Fig. 1a), which is based on unmodified 3D tomography[22]. Our simulations use viscoelastic rheologies to model intrinsic attenuation[90]. The P-wave and S-wave quality factors (Q_P and Q_S) follow established empirical relationships, assuming $Q_S = 50c_S$ (for c_S in km s^{-1}) and $Q_P = 2Q_S$ (refs. 91,92).

Off-fault plasticity

Our model accounts for nonlinear off-fault plasticity (Fig. 5b) which, in combination with near-surface velocity-strengthening behaviour, permits realistic estimates of the shallow slip deficit and near-field ground motion in the presence of complex fault geometries. We assume a non-associated Drucker–Prager elasto-viscoplastic rheology to model off-fault damage[89], parameterized by bulk internal friction coefficient and 3D variable plastic cohesion. We use a uniform bulk friction coefficient of 0.7 and define plastic cohesion C_{plast} as everywhere proportional to the 3D heterogeneous shear modulus[93] $\mu(x, y, z)$ (in Pa):

$$C_{plast} = 10^{-4}\mu(x, y, z). \quad (16)$$

The onset of plastic yielding is not instantaneous but governed by viscoplastic relaxation with a relaxation time T_v set to 0.05 s, which ensures convergence of simulation results with mesh refinement[89].

In our models, the total seismic moment $M_{0,t}$ is the sum of the moment due to slip on the fault, $M_{0,e}$, and $M_{0,p}$, the moment contribution of distributed off-fault plastic strain quantified as η, a scalar quantity measuring the accumulated off-fault plastic strain at the end of the foreshock or mainshock dynamic rupture simulations. Following previous analysis[94–97], we calculate the contribution of plastic strain to the total seismic moment as:

$$M_{0,p} = \sum_{i=1}^{N} \mu V \eta, \quad (17)$$

with μ being the rigidity, V the volume of each tetrahedral element i and

$$\eta(t) = \int_0^t \sqrt{\frac{1}{2}\dot{\epsilon}_{ij}^p \dot{\epsilon}_{ij}^p}\, \mathrm{d}t, \quad (18)$$

and $\dot{\epsilon}_{ij}^p$ being the inelastic strain rate. The contribution of plastic strain to the total moment is small but non-negligible specifically for the mainshock scenario (where $M_{0,p}/M_{0,t} \approx 8\%$).

Backprojection

To image the rupture processes of the Searles Valley foreshock and the Ridgecrest mainshock sequence, we assume a grid of possible source locations covering the latitude range 34° N to 37.5° N, and longitude range −120° W to −116° W, with 0.05° grid spacing in both latitude and longitude. We use the relatively dense array data from Alaska. Only stations with relatively high average coherence (>0.6) of the P wave are selected to avoid interference of low-quality signals and noise. We use the Ridgecrest mainshock as a reference event and apply a cross-correlation method using 20 s of P-wave onset aligned recordings, filtered between 0.1 Hz and 1 Hz to calculate the waveform coherency. Based on this, 268 stations from the Alaska array are selected. Azimuth coverage ranges from 320° to 348°, and epicentral distances range from 30° to 45°, which ensures that the P and S phases are well separated. Stations at regional distance have also been used to perform backprojection of both events[98], which is overall in agreement with our results. While regional backprojection is feasible with respect to the short duration of both earthquakes, close proximity and rupture complexity of the sequence may challenge regional backprojection resolution and stability. We use the 1D velocity model ak135[99] to calculate theoretical travel times from the source grid to each seismic station. We image the rupture process of both events using a sliding time backprojection technique, with 6-s-long time windows and 1-s time steps.

We apply a calibration method[100] to reduce location uncertainties, which are mainly due to (non-accounted for) non-constant source depths, heterogeneous 3D velocity structures and anisotropy along the source to station travel paths. For calibrating, we use 14 earthquakes larger than M_w 4.5 occurring between 4 and 12 July 2019, including the foreshock and mainshock events (Supplementary Table 3).

For the Searles Valley foreshock, we use low frequency (0.5–1 Hz) data to guarantee high coherence of the wave front. Our backprojection images rupture on F1 for 6 s and rupture on F2 within the following 6 s (Fig. 2c). We interpret that F2 rupture is initiated at the hypocentre jointly with F1 rupture, and that F2 breaks in a continuous manner away from the hypocentre. Dynamic triggering from the west side of F2 is unlikely, given the distance from the hypocentre. Rupture directivity effects from F1 towards the array may result in artificially elevated amplitudes in the filtered frequency range[101] rendering the first 6 s of rupture on F2 challenging to resolve. Backprojection results, here and in ref. 102, suggest that F1 ruptured at about 1 km s^{-1} and F2 at about

1.5 km s^{-1}. Beam power reaches its first and higher energy peak at about 2–3 s, during F1 rupture. Then energy radiation drops, aligned with F1 rupture terminating in the dynamic rupture scenario. Beam power reaches a second peak at 8–9 s after the estimated rupture onset, which resembles the dynamic rupture model reaching the southwestern end of the F2 segment.

For the Ridgecrest mainshock, the higher signal-to-noise ratio of recorded waveforms guarantees coherent signals up to 2 Hz, and allows to perform multi-frequency backprojection. Higher-frequency (1–2 Hz) backprojection shows continuous rupture from the epicentre to the southern tip of F3, whereas lower-frequency (0.1–0.5 Hz and 0.25–1 Hz) results show also reactivation of F2 (Fig. 3c). Backprojection beam power features two peaks for multiple frequency ranges. The first peak is associated with rupture on F3 to the north of the conjugate F2–F3 intersection and is more sensitive to higher frequencies. We associate the second peak with the reactivation of F2 and the rupture of the southeast segment of F3. The frequency dependence of our backprojection results is probably due to the effect of rupture directivity and rupture speed variation[101,103]. The F3 rupture in backwards-array direction towards the southeast results in lower characteristic frequency at the array because of the Doppler effect. However, a faster rupture speed can increase the characteristic frequency and counteract the Doppler effect. A faster rupture speed in the southeastern part of F3 (Supplementary Fig. 14), crossing the conjugate intersection, is also observed from local array-based backprojection[98].

Kinematic PSI

We image rupture kinematics of both events from seismic waveforms using the kinematic PSI method by ref. 19. We use all available seismic stations within 130-km distance from the fault. The rupture is assumed to propagate along prescribed fault segments at spatially variable speed. Slip rates are described as Yoffe functions[104] with spatially varying rise times. The slip distribution is parameterized using spline interpolation from a variable set of control points. The rake angles are allowed to vary smoothly. Synthetic waveforms are calculated by discretizing the segments into subfaults of 1.5 × 1 km and convolving their moment-rate functions with the respective Green's functions precalculated in the GIL7 1D velocity model[105] using Axitra[106]. We band-pass filter both data and synthetics between 0.05 Hz and 0.5 Hz.

The inverse problem is formulated in a Bayesian framework[19]. The prior probability density function on the number of slip control points k follows a reciprocal distribution, $p(k) \propto k^{-1}$. By this means, it serves as Occam's razor, preferring implicitly simple, localized slip distributions. Other priors are generally uniform (probability density function) in relatively wide ranges (for example, ±45° for the rake angle). The data uncertainty is described by a multivariate Gaussian function with a full covariance matrix. It includes a component accounting for the uncertainty of Green's functions due to imperfect description of the velocity model[107]. The posterior samples are obtained by a Markov chain Monte Carlo method, namely the parallel tempering technique[108].

We assume two planar faults for the foreshock, approximating the fault geometries of F1 and F2 for simplicity. The mainshock model includes the two fault segments F2 and F3, and honours the deflected F2 geometry. The results shown in Figs. 2b and 3b correspond to the best-fitting model and serve as an example from the ensemble of solutions obtained by the Markov chain Monte Carlo sampling.

While smooth initial conditions lead to relatively smooth slip distribution in the dynamic models, the self-adapting spatial parameterization in the kinematic models tends to localize the slip due to the Occam's razor constraint (as the data do not require otherwise). It is challenging to disentangle fault slip across conjugate fault intersections in kinematic methods due to the proximity of faults and the similar radiation pattern of, for example, right-lateral F1 and left-lateral F2 segments in the foreshock. Therefore, the uncertainty is more significant for both models in the vicinity of the conjugate fault segment intersection. For example, PSI shows a smaller fault slip on F1 around the hypocentre but slightly larger slip on F2 closer to the surface for the foreshock. Similarly, minor slip patches are rather uncertain owing to their little contribution to the waveforms. In some cases, such as the one at the northwest end of the foreshock's F1, the inferred slip might be 'projected' from coinciding secondary, unaccounted faults.

Geodetic data analysis

We obtained the processed static GPS vector data from UNAVCO (https://www.unavco.org/highlights/2019/ridgecrest.html). We compare our modelled surface displacements at selected stations with observational data as shown in Figs. 2f and 3f. To avoid contamination by remnant seismic waves propagating throughout the model domain, we extract the synthetic surface displacements at 100 s after dynamic rupture nucleation in both foreshock and mainshock models. We calculate the maximal possible value of cross-correlation (CC) between the observed and synthetic time series component-wise to account for the different signal-to-noise ratios in the horizontal and vertical components.

Our modelled coseismic GPS displacements of the Searles Valley foreshock match observational recordings well at most stations, with notable overshooting amplitudes at near-fault stations CCCC and P595 (Fig. 2f). For the mainshock, we also observe overall good agreement except for small overshooting displacements at stations P595, P580 and P594 (Fig. 3f). Stations CCCC and P595 are close to the terminations of faults in our prescribed fault geometry, and the observed discrepancies may reflect a more gradual rupture arrest along F2 than captured in our model. Additional discrepancies may by associated with secondary faults off the main fault identified with optical imaging[33,58] but not explicitly incorporated in our model.

Teleseismic waveforms

We generate synthetic broadband seismograms at six teleseismic stations (of the IU network[109]) around the events (Fig. 1a and Supplementary Fig. 9) using the Instaseis[110] Green's function database and the preliminary reference Earth model (PREM)[111] incorporating anisotropic effects[112] and accurate to a shortest period of 2 s. The sources for the synthetic teleseismic waveforms are calculated by translating the fault slip time histories of the foreshock and mainshock dynamic rupture models into a respective double-couple point source, which we then use in Instaseis. The observed teleseismic data were downloaded from IRIS (Incorporated Research Institutions for Seismology) using Obspy[113].

The teleseismic synthetics fit the foreshock (Supplementary Fig. 9a; average cross-correlation coefficient of about 0.73) and mainshock (Supplementary Fig. 9b; average cross-correlation coefficient of about 0.75) observations well in the long-period range considered (50–500 s). The simplifying choice of a 1D PREM-based teleseismic Green's function database may explain some of the remaining differences.

Data availability

All data required to reproduce the earthquake sequence scenarios can be downloaded from https://zenodo.org/record/6842773. We provide a detailed README file summarizing the data and data formats provided. Our 3D fault model is available at https://skfb.ly/oDVGw. The static GPS data related to the coseismic rupture of both the foreshock and mainshock are available from UNAVCO (https://www.unavco.org/highlights/2019/ridgecrest.html). The continuous GPS dataset[35] is available at https://zenodo.org/record/3366342. The Instaseis Green's function database that we use to compute teleseismic synthetics is hosted by IRIS at https://ds.iris.edu/ds/products/syngine/. Source data are provided with this paper.

Code availability

All dynamic rupture simulations were performed using SeisSol (www.seissol.org), an open-source software freely available to download from https://github.com/SeisSol/SeisSol/. The used SeisSol code branch and commit are archived at https://zenodo.org/record/7642533. The SeisSol Ridgecrest sequence branch is also available on GitHub (https://github.com/SeisSol/SeisSol/tree/2019_Ridgecrest_sequence). Instructions for downloading, installing and running the code are available in the SeisSol documentation at https://seissol.readthedocs.io/. Downloading and compiling instructions are at https://seissol.readthedocs.io/en/latest/compiling-seissol.html. Instructions for setting up and running simulations are at https://seissol.readthedocs.io/en/latest/configuration.html. Quickstart containerized installations and introductory materials are provided in the docker container and jupyter notebooks at https://github.com/SeisSol/Training. Example problems and model configuration files are provided at https://github.com/SeisSol/Examples, many of which reproduce the SCEC 3D Dynamic Rupture benchmark problems described at https://strike.scec.org/cvws/benchmark_descriptions.html. We use the software SKUA-GOCAD (https://www.aspentech.com/en/resources/brochure/aspen-skua) as the modelling environment to produce all 3D fault models and the open-source software ParaView (https://www.paraview.org/) for visualization.

45. Dumbser, M. & Käser, M. An arbitrary high-order discontinuous Galerkin method for elastic waves on unstructured meshes—II. The three-dimensional isotropic case. *Geophys. J. Int.* **167**, 319–336 (2006).
46. Breuer, A. et al. Sustained petascale performance of seismic simulations with SeisSol on SuperMUC. In *Supercomputing. ISC 2014. Lecture Notes in Computer Science* Vol. 8488, 1–18 (Springer, 2014).
47. Heinecke, A. et al. Petascale high order dynamic rupture earthquake simulations on heterogeneous supercomputers. In *International Conference for High Performance Computing, Networking, Storage and Analysis, SC* 3–14 (IEEE, 2014).
48. Rettenberger, S., Meister, O., Bader, M. & Gabriel, A.-A. Asagi: a parallel server for adaptive geoinformation. In *Proc. Exascale applications and Software Conference 2016*, 2:1–2:9 (ACM, 2016).
49. Uphoff, C. et al. Extreme scale multi-physics simulations of the tsunamigenic 2004 Sumatra megathrust earthquake. In *Proc. International Conference for High Performance Computing, networking, Storage and Analysis, SC 2017* (2017).
50. Krenz, L. et al. 3D acoustic-elastic coupling with gravity: the dynamics of the 2018 Palu, Sulawesi earthquake and tsunami. In *Proc. International Conference for High Performance Computing, Networking, Storage and Analysis, SC'21* 1–17 (ACM, N2021).
51. Pelties, C., Gabriel, A.-A. & Ampuero, J.-P. Verification of an ADER-DG method for complex dynamic rupture problems. *Geosci. Model Dev.* **7**, 847–866 (2014).
52. Harris, R. A. et al. Verifying a computational method for predicting extreme ground motion. *Seismol. Res. Lett.* **82**, 638–644 (2011).
53. Harris, R. A. et al. A suite of exercises for verifying dynamic earthquake rupture codes. *Seismol. Res. Lett.* **89**, 1146–1162 (2018).
54. Valkaniotis, S. Subpixel optical correlation co-seismic offsets for the M_w 6.4 and M_w 7.1 Ridgecrest, California earthquakes, from Copernicus Sentinel 2 data. *Zenodo* https://doi.org/10.5281/zenodo.3275073 (2019).
55. Planet Data Application Program Interface. in *Space for Life On Earth* (Planet, 2019); https://www.planet.com/markets/education-and-research/.
56. Wang, X. & Zhan, Z. Seismotectonics and fault geometries of the 2019 Ridgecrest sequence: insight from aftershock moment tensor catalog using 3-D Green's functions. *J. Geophys. Res. Solid Earth* **124**, e2020JB019577 (2020).
57. Plesch, A., Shaw, J. H., Ross, Z. E. & Hauksson, E. Detailed 3D fault representations for the 2019 Ridgecrest, California, earthquake sequence. *Bull. Seismol. Soc. Am.* **110**, 1818–1831 (2020).
58. Xu, X., Sandwell, D. T. & Smith-Konter, B. Coseismic displacements and surface fractures from Sentinel-1 InSAR: 2019 Ridgecrest earthquakes. *Seismol. Res. Lett.* **91**, 1979–1985 (2020).
59. Dunham, E. M., Belanger, D., Cong, L. & Kozdon, J. E. Earthquake ruptures with strongly rate-weakening friction and off-fault plasticity, part 1: planar faults. *Bull. Seismol. Soc. Am.* **101**, 2296–2307 (2011).
60. Heaton, T. H. Evidence for and implications of self-healing pulses of slip in earthquake rupture. *Phys. Earth Planet. Inter.* **64**, 1–20 (1990).
61. Nielsen, S. & Madariaga, R. On the self-healing fracture mode. *Bull. Seismol. Soc. Am.* **93**, 2375–2388 (2003).
62. Dieterich, J. H. Modeling of rock friction: 1. Experimental results and constitutive equations. *J. Geophys. Res. Solid Earth* **84**, 2161–2168 (1979).
63. Ruina, A. Slip instability and state variable friction laws. *J. Geophys. Res. Solid Earth* **88**, 10359–10370 (1983).
64. Blanpied, M. L., Lockner, D. A. & Byerlee, J. D. Fault stability inferred from granite sliding experiments at hydrothermal conditions. *Geophys. Res. Lett.* **18**, 609–612 (1991).
65. Wei, M., Kaneko, Y., Liu, Y. & McGuire, J. J. Episodic fault creep events in California controlled by shallow frictional heterogeneity. *Nat. Geosci.* **6**, 566–570 (2013).
66. Kaneko, Y., Lapusta, N. & Ampuero, J.-P. Spectral element modeling of spontaneous earthquake rupture on rate and state faults: effect of velocity-strengthening friction at shallow depths. *J. Geophys. Res. Solid Earth* **113**, B09317 (2008).
67. Tinti, E. et al. Constraining families of dynamic models using geological, geodetic and strong ground motion data: the M_w 6.5, October 30th, 2016, Norcia earthquake, Italy. *Earth Planet Sci. Lett.* **576**, 117237 (2021).
68. Anderson, E. M. The dynamics of faulting. *Trans. Edinb. Geol. Soc* **8**, 387–402 (1905).
69. Aochi, H. & Madariaga, R. The 1999 Izmit, Turkey, earthquake: nonplanar fault structure, dynamic rupture process, and strong ground motion. *Bull. Seismol. Soc. Am.* **93**, 1249–1266 (2003).
70. Suppe, J. Fluid overpressures and strength of the sedimentary upper crust. *J. Struct. Geol.* **69**, 481–492 (2014).
71. Madden, E. H., Ulrich, T. & Gabriel, A.-A. The state of pore fluid pressure and 3-D megathrust earthquake dynamics. *J. Geophys. Res. Solid Earth* **127**, e2021JB023382 (2022).
72. Hauksson, E. et al. Preliminary report on the 1995 Ridgecrest earthquake sequence in Eastern California. *Seismol. Res. Lett.* **66**, 54–60 (1995).
73. Verdecchia, A. & Carena, S. One hundred and fifty years of Coulomb stress history along the California–Nevada border, USA: Coulomb stress history CA–NV border. *Tectonics* **34**, 213–231 (2015).
74. Rubin, A. M. & Ampuero, J.-P. Earthquake nucleation on (aging) rate and state faults. *J. Geophys. Res. Solid Earth* **110**, B11312 (2005).
75. Lapusta, N. & Liu, Y. Three-dimensional boundary integral modeling of spontaneous earthquake sequences and aseismic slip. *J. Geophys. Res. Solid Earth* **114**, B09303 (2009).
76. Jiang, J. & Lapusta, N. Deeper penetration of large earthquakes on seismically quiescent faults. *Science* **352**, 1293–1297 (2016).
77. Luo, B., Duan, B. & Liu, D. 3D finite-element modeling of dynamic rupture and aseismic slip over earthquake cycles on geometrically complex faults. *Bull. Seismol. Soc. Am.* **110**, 2619–2637 (2020).
78. Meng, Q. & Duan, B. Dynamic modeling of interactions between shallow slow-slip events and subduction earthquakes. *Seismol. Soc. Am.* **94**, 206–216 (2023).
79. Jiang, J. et al. Community-driven code comparisons for three-dimensional dynamic modeling of sequences of earthquakes and aseismic slip. *J. Geophys. Res. Solid Earth* **127**, e2021JB023519 (2022).
80. Uphoff, C., May, D. A. & Gabriel, A.-A. A discontinuous Galerkin method for sequences of earthquakes and aseismic slip on multiple faults using unstructured curvilinear grids. *Geophys. J. Int.* **233**, 586–626 (2022).
81. Andrews, D. Rupture models with dynamically determined breakdown displacement. *Bull. Seismol. Soc. Am.* **94**, 769–775 (2004).
82. Bizzarri, A. How to promote earthquake ruptures: different nucleation strategies in a dynamic model with slip-weakening friction. *Bull. Seismol. Soc. Am.* **100**, 923–940 (2010).
83. Hu, F., Huang, H. & Chen, X. Effect of the time-weakening friction law during the nucleation process. *Earthq. Sci.* **30**, 91–96 (2017).
84. Harris, R. A. et al. A geology and geodesy based model of dynamic earthquake rupture on the Rodgers Creek–Hayward–Calaveras fault system, California. *J. Geophys. Res. Solid Earth* **126**, e2020JB020577 (2021).
85. Galis, M. et al. On the initiation of sustained slip-weakening ruptures by localized stresses. *Geophys. J. Int.* **200**, 890–909 (2015).
86. Freund, L. B. *Dynamic Fracture Mechanics* (Cambridge Univ. Press, 1998).
87. Hardebeck, J. L. & Michael, A. J. Damped regional-scale stress inversions: methodology and examples for Southern California and the Coalinga aftershock sequence. *J. Geophys. Res. Solid Earth* **111**, B11310 (2006).
88. Farr, T. G. et al. The Shuttle Radar Topography Mission. *Rev. Geophys.* **45**, RG2004 (2007).
89. Wollherr, S., Gabriel, A.-A. & Uphoff, C. Off-fault plasticity in three-dimensional dynamic rupture simulations using a modal discontinuous Galerkin method on unstructured meshes: implementation, verification and application. *Geophys. J. Int.* **214**, 1556–1584 (2018).
90. Uphoff, C. & Bader, M. Generating high performance matrix kernels for earthquake simulations with viscoelastic attenuation. In *2016 International Conference on High Performance Computing & Simulation (HPCS)* 908–916 (IEEE, 2016).
91. Day, S. M. & Bradley, C. R. Memory-efficient simulation of anelastic wave propagation. *Bull. Seismol. Soc. Am.* **91**, 520–531 (2001).
92. Graves, R. W. et al. Broadband simulations for M_w 7.8 southern San Andreas earthquakes: ground motion sensitivity to rupture speed. *Geophys. Res. Lett.* **35**, L22302 (2008).
93. Roten, D., Olsen, K. B., Day, S. M., Cui, Y. & Fäh, D. Expected seismic shaking in los angeles reduced by San Andreas Fault zone plasticity. *Geophys. Res. Lett.* **41**, 2769–2777 (2014).
94. Andrews, D. J. Rupture dynamics with energy loss outside the slip zone. *J. Geophys. Res. Solid Earth* **110**, B01307 (2005).
95. Ma, S. A physical model for widespread near-surface and fault zone damage induced by earthquakes. *Geochem. Geophys. Geosyst.* **9**, Q11009 (2008).
96. Gabriel, A.-A., Ampuero, J.-P., Dalguer, L. A. & Mai, P. M. Source properties of dynamic rupture pulses with off-fault plasticity. *J. Geophys. Res. Solid Earth* **118**, 4117–4126 (2013).
97. Ulrich, T., Gabriel, A.-A. & Madden, E. H. Stress, rigidity and sediment strength control megathrust earthquake and tsunami dynamics. *Nat. Geosci.* **15**, 67–73 (2022).
98. Xie, Y., Bao, H. & Meng, L. Source imaging with a multi-array local back-projection and its application to the 2019 M_w 6.4 and M_w 7.1 Ridgecrest earthquakes. *J. Geophys. Res. Solid Earth* **126**, e2020JB021396 (2021).
99. Kennett, B. L. N. & Engdahl, E. R. Traveltimes for global earthquake location and phase identification. *Geophys. J. Int.* **105**, 429–465 (1991).
100. Ghosh, A., Vidale, J. E. & Creager, K. C. Tremor asperities in the transition zone control evolution of slow earthquakes. *J. Geophys. Res. Solid Earth* **117**, B10301 (2012).
101. Li, B. et al. Rupture heterogeneity and directivity effects in back-projection analysis. *J. Geophys. Res. Solid Earth* **127**, e2021JB022663 (2022).
102. Yang, J., Zhu, H. & Lumley, D. Time-lapse imaging of coseismic ruptures for the 2019 Ridgecrest earthquakes using multiazimuth backprojection with regional seismic data and a 3-D crustal velocity model. *Geophys. Res. Lett.* **47**, e2020GL087181 (2020).

103. Yin, J. & Denolle, M. A. Relating teleseismic backprojection images to earthquake kinematics. *Geophys. J. Int.* **217**, 729–747 (2019).
104. Tinti, E., Fukuyama, E., Piatanesi, A. & Cocco, M. A kinematic source-time function compatible with earthquake dynamics. *Bull. Seismol. Soc. Am.* **95**, 1211–1223 (2005).
105. Pasyanos, M. E., Dreger, D. S. & Romanowicz, B. Toward real-time estimation of regional moment tensors. *Bull. Seismol. Soc. Am.* **86**, 1255–1269 (1996).
106. Cotton, F. & Coutant, O. Dynamic stress variations due to shear faults in a plane-layered medium. *Geophys. J. Int.* **128**, 676–688 (1997).
107. Hallo, M. & Gallovič, F. Fast and cheap approximation of Green function uncertainty for waveform-based earthquake source inversions. *Geophys. J. Int.* **207**, 1012–1029 (2016).
108. Sambridge, M. A parallel tempering algorithm for probabilistic sampling and multimodal optimization. *Geophys. J. Int.* **196**, 357–374 (2013).
109. Albuquerque Seismological Laboratory/USGS. Global Seismograph Network (GSN - IRIS/USGS) [data set]. *International Federation of Digital Seismograph Networks* https://doi.org/10.7914/SN/IU (2014).
110. van Driel, M., Krischer, L., Stähler, S., Hosseini, K. & Nissen-Meyer, T. Instaseis: instant global seismograms based on a broadband waveform database. *Solid Earth* **6**, 701–717 (2015).
111. Dziewonski, A. M. & Anderson, D. L. Preliminary reference Earth model. *Phys. Earth Plan. Int.* **25**, 297–356 (1981).
112. Mégnin, C. & Romanowicz, B. The three-dimensional shear velocity structure of the mantle from the inversion of body, surface and higher-mode waveforms. *Geophys. J. Int.* **143**, 709–728 (2000).
113. Krischer, L. et al. ObsPy: a bridge for seismology into the scientific Python ecosystem. *Comput. Sci. Discov.* **8**, 014003 (2015).

Acknowledgements We thank M. Bader, L. Krenz, S. Wolf, R. Dorozhinskii and the group of hardware-aware algorithms and software for high-performance computing at TUM for decade-long collaboration; N. Schliwa, J. Biemiller, C. Nicholson and S. A. Wirp for discussions; and S. Antoine for sharing surface offset data. This work was supported by the European Union's Horizon 2020 Research and Innovation Programme (TEAR grant number 852992) and Horizon Europe (ChEESE-2P grant number 101093038, DT-GEO grant number 101058129 and Geo-INQUIRE grant number 101058518), the National Science Foundation (grant number EAR-2121666), the German Research Foundation (DFG projects GA 2465/2-1 and GA 2465/3-1) and the Southern California Earthquake Center (SCEC award 21112). We acknowledge the Gauss Centre for Supercomputing e.V. (www.gauss-centre.eu) for providing computing time on the GCS Supercomputer SuperMUC-NG at Leibniz Supercomputing Centre (www.lrz.de), in project pr63qo.

Author contributions Conceptualization, formal analysis, software, visualization and writing: T.T., A.-A.G., D.L., T.U., B.L., S.C., A.V. and F.G. Funding acquisition and resources: A.-A.G..

Competing interests The authors declare no competing interests.

Additional information

Supplementary information The online version contains supplementary material available at https://doi.org/10.1038/s41586-023-05985-x.

Correspondence and requests for materials should be addressed to Alice-Agnes Gabriel.

Peer review information *Nature* thanks the anonymous reviewers for their contribution to the peer review of this work. Peer reviewer reports are available.